THE MESSENGER

EL MENSAJERO

Munich
Paranal
La Silla
La Serena
Santiago

No. 97 – September 1999

TELESCOPES AND INSTRUMENTATION

News from the VLT

M. TARENGHI, ESO

During the last months, the work at ESO's Very Large Telescope (VLT) project, both at the Paranal Observatory and in Europe, progressed very well. On the following pages is a brief description of the recent achievements and the activities that will take place in the next months.

Figure 1: From the window of a commercial airplane on a flight from Santiago to Antofagasta, G. Wayne Van Citters from NSF took this dramatic photo of the Atacama desert. In the isolation of the mountain desert the constructions of the Paranal Observatory resemble a "mirage".

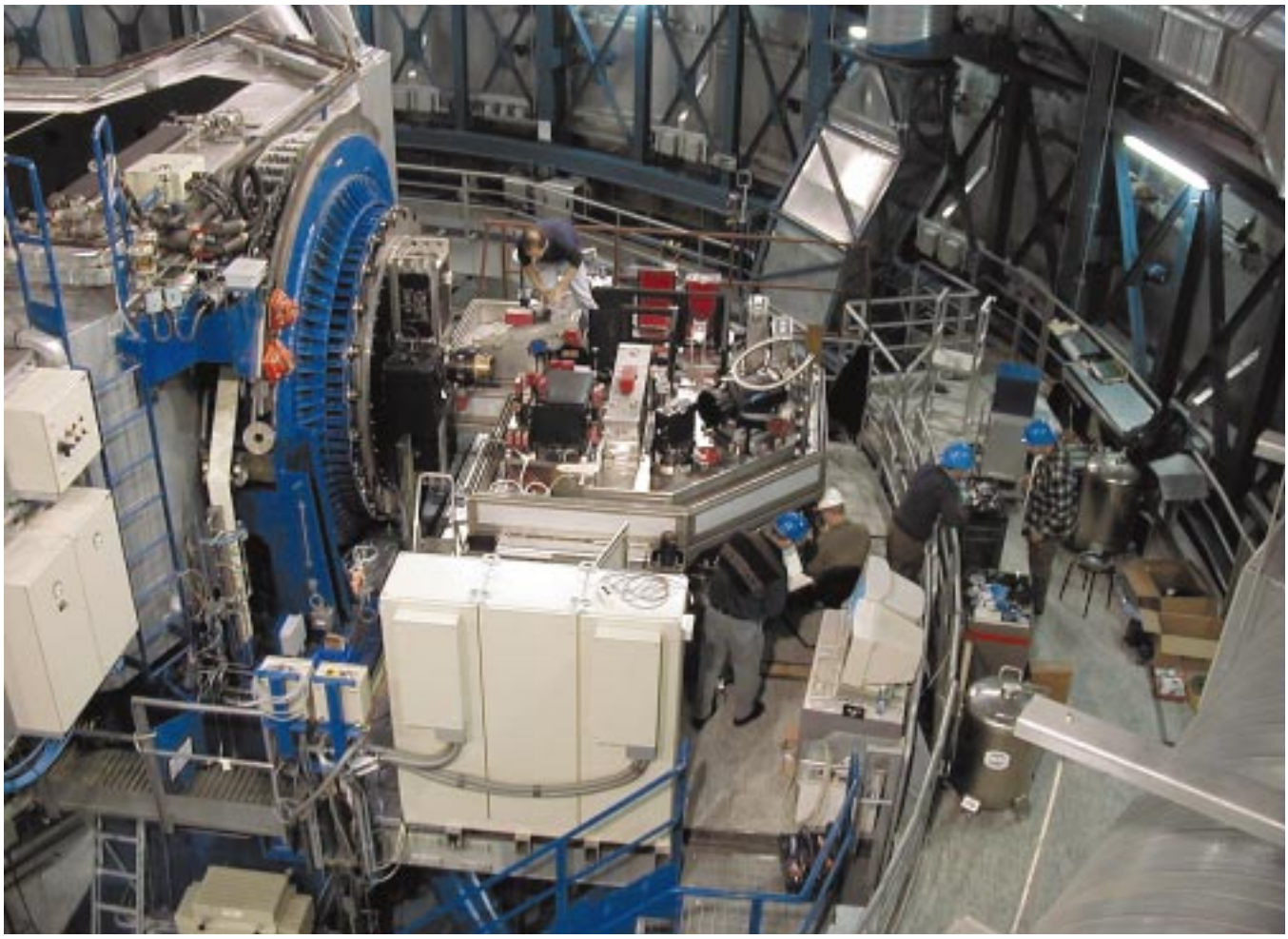

Figure 2: UVES. General view from above the KUEYEN Nasmyth platform where the high-resolution UVES spectrograph is being installed. The rotator-adapter is to the left, within the blue-painted support. (This digital photo was obtained on September 2, 1999.)

ANTU (UT1)

It is now half a year since 1st April when the first 8.2-m VLT Unit Telescope (ANTU) was handed over to the astronomers and it started to deliver excellent observational data. More than 35,000 scientific frames have been obtained so far with FORS and ISAAC. Many of the images have a seeing better than 0.4 arcsec. Several research projects for which time was allocated during the past months have reported very good and even spectacular results. In some cases, the data were fully reduced and the astronomers involved are now in the final stages of preparing the associated scientific reports and papers. Our scientific operation team guided by R. Gilmozzi gained enormous experience both in the service and visitor modes. Now it is time to transfer the telescopes and instruments to the others. A fundamental contribution was given by the Garching front end and back end operations teams led by D. Silva and B. Leibundgut that interact with the community in the preparation of the observation and the support of the VLT archive.

KUEYEN (UT2)

Following "First Light" in March this year, the commissioning work for the second Unit Telescope successfully reached a milestone when instruments could be integrated at the different

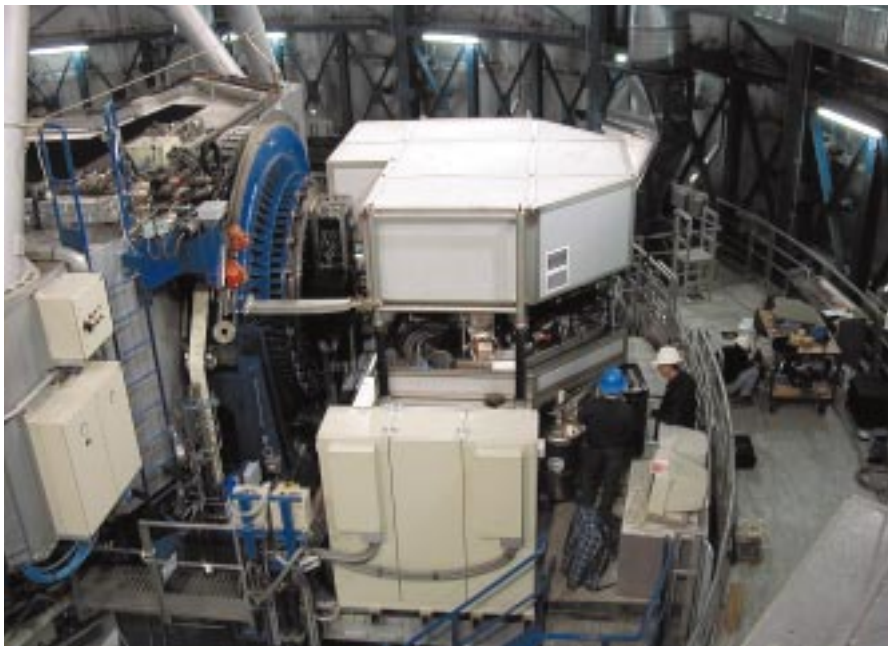

Figure 3: UVES. When the UVES cover is put in place, it protects the sensitive inner parts of the instrument from unwanted light and dust. (This digital photo was obtained on September 16, 1999.)

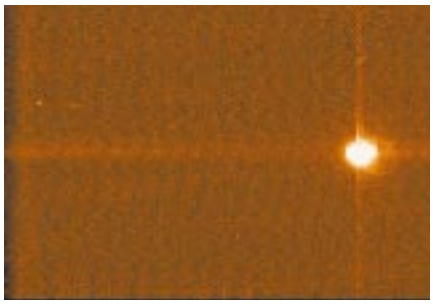

Figure 4: UT3 first pointing. First image of a star obtained with the CCD camera at the 20-cm guide telescope on MELIPAL, at the beginning of pointing and tracking tests.

telescope foci. The KUEYEN Commission Team, led by Jason Spyromilio, tuned the telescope control system in such a way that the pointing tests are proceeding extremely well. During a series of 145 test stars just completed and covering the entire operating range of the telescope, on no occasion was the star out of the patch. From the real performance measurements, the overall RMS value was found to be only 0.85 arcsec and no stars were rejected during the test. This is an excellent result for any telescope.

The next major activity, currently underway, is the mounting of the large, high-dispersion spectrograph UVES onto one of the Nasmyth platforms (see Figs. 2 and 3). UVES is the second major VLT instrument to be built at ESO. It is also one of the heaviest and most complex ones at this astronomical facility. This delicate work includes the installation and exceedingly accurate alignment of the many optical components on the heavy base plate, necessary to ensure the highest optical quality during the forthcoming observations. The moment of "UVES First Light" with the first test observations of spectra of celestial objects is expected the last week of September.

Figure 5: Mirror cell for UT4. The fourth M1 Cell (for YEPUN) in its protective cover arrives at Paranal, after a safe passage from Europe. (This digital photo was obtained on August 23, 1999).

Work on the assembly of FORS2 continued at the Integration Laboratory in the Mirror Maintenance Building (MMB) and the first tests were made. This instrument will be installed at the Cassegrain focus of KUEYEN in late October 1999.

MELIPAL (UT3)

The dummy M1 mirror cell was removed in early August from the third Unit Telescope (MELIPAL) and the real Mirror Cell (the third "M1 Cell"), although still with a concrete (dummy) mirror, was installed at the telescope. With a dummy M2 Unit in place at the top of the telescope frame, pointing and tracking tests were initiated. The first image with the 20-cm guide telescope mounted on the centrepiece and used for these tests was obtained in late August (see Fig. 4). As was the case for the first two Unit Telescopes, the mechanical quality of MELIPAL was found to be excellent and the pointing has now been tuned to a few arcsec over the entire sky. The tracking is also very good. Following these tests, the M1 Cell was again taken down to the MMB at the Base Camp and the dummy concrete mirror was removed. The M1 Cell was moved back up the mountain and stored under the MELIPAL structure until the (third) 8.2-m Zerodur mirror is installed in mid-November. "First light" with the VLT Test Camera at the Cassegrain focus of this telescope is planned for February 2000.

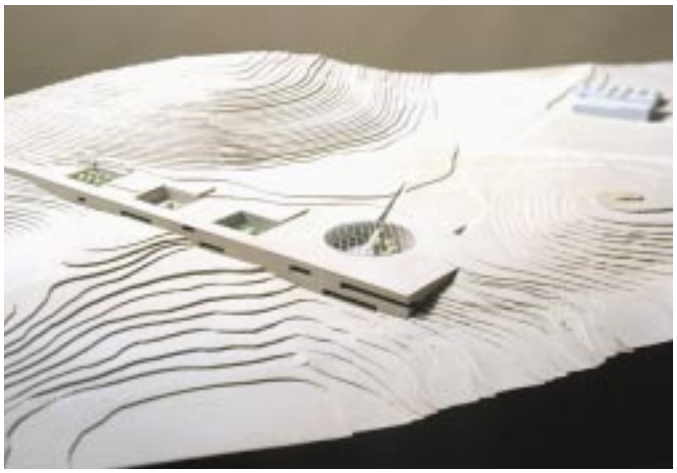

Figure 6: "Residencia" model. Photo of the architect's model of the Paranal Residencia and Offices. The building is fully integrated into the landscape. Its southern and western facades emerge from the ground, providing a view from the bedrooms, offices and restaurant towards the Pacific Ocean.

Figure 7: Start of construction. View of the building site where the first part of the new Paranal Residencia and Offices are now under construction.

YEPUN (UT4)

The fourth Unit Telescope (YEPUN) is now in the final phase of mechanical assembly. Acceptance tests with the supplier will start soon, after which the construction of the four telescope structures will have been finished. The fourth M1 Cell arrived at Paranal in late August (Fig. 5). "First Light" for YEPUN is scheduled for July 2000.

VLTI

In Europe, major achievements occurred in the area of the VLT Interferometer (VLTI) construction. The two siderostats are being tested on the cloudy European sky (see article by F. Derie et al. in this issue). ESO concluded a contract with REOSC (France) for delivery of all mirrors to equip the four VLT Unit Telescopes with coudé foci optics. An important milestone was reached with the completion of the polishing of the optics for the first delay line for the VLTI at REOSC. The integration of the cat's eye will be done at TNO (Netherlands) and this part will then be integrated into the delay line at Fokker Aerospace (The Netherlands). Shipment to Chile will take place immediately afterwards. In addition, the 1.8-m primary mirror for the first VLTI Auxiliary Telescope has reached the final stage of the light-weighting process and the optical polishing will soon begin at AMOS (Belgium). The already manufactured optics (null correctors, M2 matrix) have shown excellent optical quality results. A contract for the purchasing of the Auxiliary Telescope number 3 was concluded with AMOS.

The "Residencia"

It has always been ESO's intention to provide better quarters and living facilities at Paranal. Plans for the design and construction of the "Facilities for Offices, Board and Lodging", also known as the Paranal Residencia and Offices, were therefore begun some years ago. The project was developed by Auer and Weber Freie Architekten from Munich (Germany). Their design was selected among eight proposals from European and Chilean architects.

The unusual conceptual design is structured as an L-shaped building, located downhill from the Paranal access road on the southwest side of the present Base Camp. The building is fully integrated into the landscape, essentially underground with its southern and western facades emerging from the ground, providing a view from the bedrooms, offices and restaurant towards the Pacific Ocean. The common facilities, restaurant, offices, library, reception and meeting rooms are articulated around the corner of the building, while the hotel rooms are distributed along the wings of the L-shape. A circular hall, 35 m wide and four floors deep – covered with a dome emerging at ground level – is the building's focal point with natural light. At the floor of the hall there is an oasis of vegetation with a swimming pool. Special protection against light pollution is foreseen. To a large extent, the ventilation is with natural airflow through remotely controlled air in outlets.

The Chilean firm Vial y Vives won the construction tender. Work on the first part of the building began on July 1, 1999, and is scheduled to be completed within two years. The excavation work for the Paranal Residencia is proceeding according to schedule, with the first concrete to be cast shortly.

Performance of the VLT Mirror Coating Unit

E. ETTLINGER (LINDE), P. GIORDANO and M. SCHNEERMANN (ESO)

In August 1995 ESO signed a contract with LINDE AG to supply the coating unit for the mirrors of the Very Large Telescope. The coating unit was first erected and tested in Germany and then disassembled, packed and shipped to Chile. After integration into the Main Maintenance Building on Paranal, the first mirror was coated on May 20, 1998 ("First Light" on May 25–26, 1998). The final runs for provisional acceptance were performed in January 1999.

The Coating Unit

The Coating Unit encloses the following main components (see Fig. 1):

- the vacuum chamber with a diameter of more than 9 m and an inner volume of 122 m^3
- the roughing pump system and the high vacuum pumping system, consisting of 8 cryo pumps and a Meissner trap
- the mirror support system, a whiffle tree structure with lateral and axial pads to support the glass mirror during coating
- the mirror rotary device including a ferrofluidic vacuum feedthrough, to rotate the mirror underneath the magnetron during coating
- the coating cart, enclosing an air cushion system to drive the lower chamber section and a lifting device, to close the vacuum chamber after mirror loading
- the magnetron sputter source with a water-cooled shutter system and cryogenic shields
- the glow discharge cleaning device, to heat up and clean the mirror surface prior to coating.

Thin Film Deposition Equipment

The main component for the coating process is the thin film deposition equipment of the Coating Unit comprising the following components:

- sputter source for aluminium including power supply
- shields to trim the aluminium coating deposited
- shutter panels
- cryo panels attached to the shutters
- Glow Discharge Cleaning Device (GDCD) including power supplies

The DC Planar Magnetron Source consists of the target 99.995% pure aluminium cathode bonded to a water-cooled backing plate to reduce the heat radiated to the mirror. The discharge is produced by the use of an inert gas (Argon) to support the flow of current between cathode and anode. The planar magnetron source uses magnetic fields to focus electrons in the region of the sputtering target.

Stainless steel trim shields, which are placed below the cathode to trim the deposition of the sputtered aluminium, ensure that the mirror is evenly coated with a uniform thickness of aluminium.

The shutter panels are stainless steel sheet box constructions, which are cooled by water, fed through the panels under pressure. There are two shutters, one to form the leading edge of the coating, and one to form the trailing edge. Both shutters are pivoted about the centre of the mirror, and at the beginning of a coating run both shutters are closed together along the line of the joint band.

Below the shutter panels, copper cryo panels are suspended, filled with liquid nitrogen.

Their purpose is to provide an area of high purity and homogeneity between the shutter opening below the magnetron and hence aid and improve the quality of the reflectance of the aluminium deposited onto the mirror.

The GDCD consists of two aluminium electrodes, shaped to give the required profile. The glow discharge electrodes are water-cooled and are suspended from a dark space shield, which is also made of aluminium. The purpose of the GDCD is to reduce adsorbed water molecules from the mirror, the inner surfaces of the chamber and all components mounted inside the chamber. The

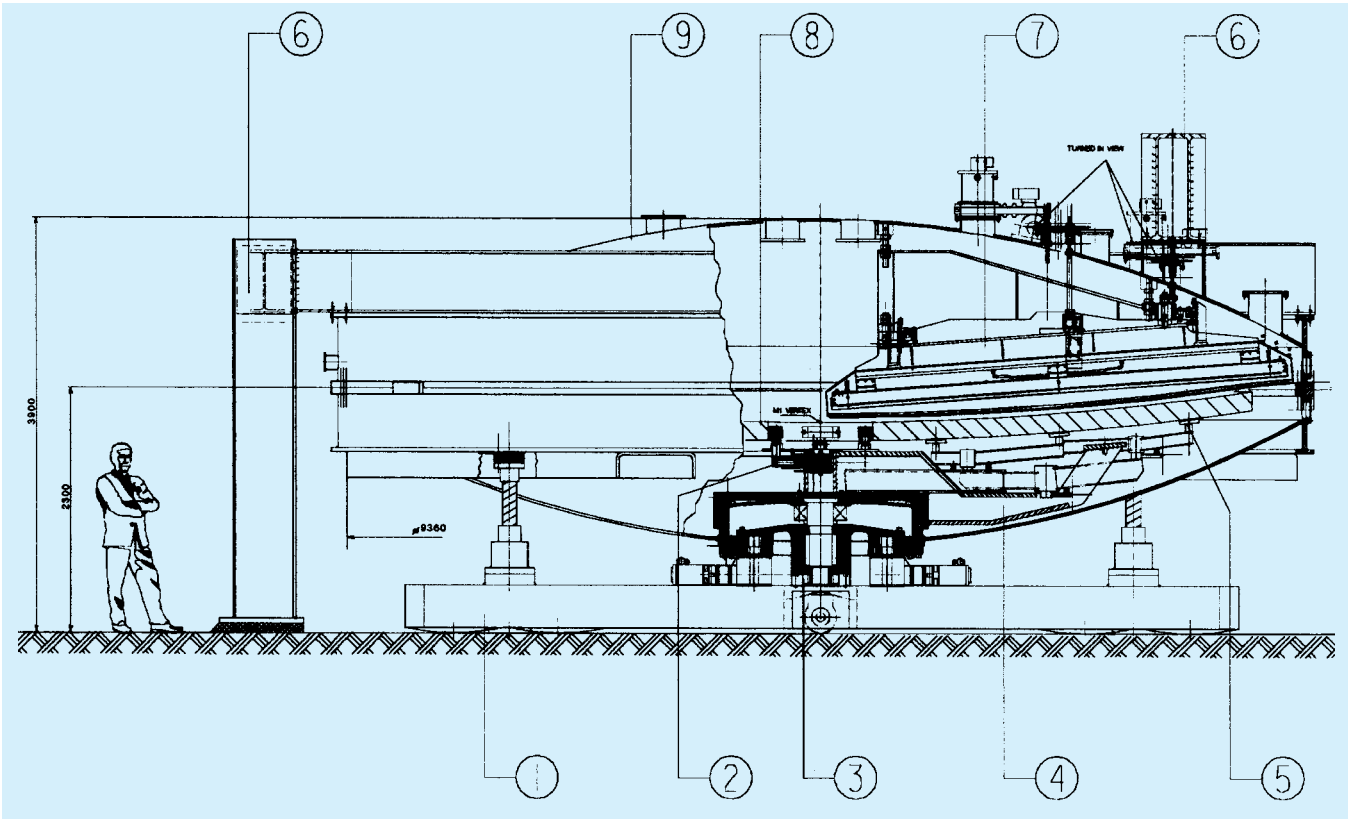

Figure 1: Main components of the VLT Coating Unit. Cart chassis and drive (1), Lateral pads (2), Mirror rotary device (3), Mirror support system (4), Axial pads (5), Supporting frame (6), Magnetron, shield and shutter (7), M1 mirror (8), Vacuum vessel (9).

glow discharge also heats the mirror surface, which improves film adhesion and film purity.

Process Description

The method selected to deposit a thin aluminium film on the mirror is the sputtering process.

The sputter coating process is done by inserting a mirror into a vacuum chamber, which contains a specially designed cathode and an inert process gas. A negative voltage is applied to the cathode (target) and a glow discharge (plasma) ignites within the vacuum chamber when the appropriate environment (or conditions) are achieved.

At this point, positively charged atoms of the gas (ions) are attracted to the surface of the target which is negatively charged. The positive atoms strike the negatively charged target with such force that atoms of the target are ejected and deposited on the mirror surface, building up a thin layer atom by atom.

What differentiates a magnetron cathode (used here) from a conventional diode cathode is the presence of a magnetic field which confines electrons in the region of the sputtering target. A magnetic field is supplied from below the cathode target, which is arranged so that free electrons are captured in the crossed magnetic and electric fields in the region. The captured electrons enhance the ionisation in the inert gas atmosphere. Overall, the effect is to lower the operating voltage required, from several kilovolts to less than 1000 volts. The most striking gain of the magnetron design, however, is an order-of-magnitude increase in coating deposition rates per unit area of target.

Figure 2: The lower part of the coating unit vacuum chamber. For loading and unloading of the mirrors, the lower half of the chamber is moved on 8 air-cushions from the coating unit location to the mirror handling tool and vice versa.

Coating Procedure

The mirror is loaded into the lower half of the coating unit. The two halves of the vacuum chamber are brought together, sealing the coating unit. Then the chamber is pumped down to achieve the required vacuum level.

The mirror is rotated beneath the sputter source and GDCD so that it can first receive a surface treatment and then its coating of Aluminium.

After the surface treatment via the GDCD has been completed the magnetron is powered up to pre-sputter until the cathode's surface is clean.

The mirror is rotated at a pre-determined speed calculated to give the intended coating thickness at the intended

Figure 3: A look into the coating unit vacuum chamber. The upper vacuum chamber part carries the DC planar magnetron sputter source. In the lower part the rotatable whiffle tree for support of the primary mirror is visible.

sputtering rate. The leading edge shutter is opened as the intended position of the joint band passes underneath. Thereby, the rotational speed of the shutter exactly matches that of the mirror.

After the mirror has completed one revolution, the trailing edge shutter is closed by rotating it at the same rotational speed as the mirror, as the film joint passes underneath. This produces sharply stepped edges to the coating, the trailing edge lying on top of the leading edge. Shadowing of the coating by the shutter edges prevents them from being perfect steps.

Because both shutters are pivoted about the centre of the mirror, all points along the joint band take the same time to cross the mirror opening.

Figure 4 shows an overview of the pressure conditions inside the coating chamber during the glow discharge cleaning treatment of the mirror and the sputter process. Prior to glow discharge cleaning, the chamber is pumped down to less than 0.001 Pa. Then air is fed in and at a pressure of 2 Pa (cryo pumps throttled) the GDC process is started. After the mirror has completed one revolution, the glow discharge cleaning is finished and the chamber is pumped down to less than 0.0002 Pa within less than 10 minutes, which demonstrates the high pumping speed of the high-vacuum pumping system. Finally, argon is fed in and sputtering is started at an argon pressure of 0.08 Pa.

Test Procedure

During the tests of the coating unit the M1 mirror was replaced by the dummy substrate, a test platform which represents the surface of the M1 mirror. It allowed the mounting of glass slides (50 × 50 mm, 1 mm thick) onto which the aluminium coating was deposited.

Up to 60 glass slides were mounted onto the dummy substrate at intervals along the M1 radius. The position of the slides was recorded on the back of the slides, together with the coating run number.

During a long experimental phase, which covered more than 30 test runs, the following parameters were optimised:

- pressure of the argon process gas
- clearance between aluminium target and mirror surface
- adjustment of shutter for an extremely small joint line
- rotation speed of mirror rotary device.

The influence of the glow discharge cleaning device was investigated with respect to the film adhesion and reflectivity of the samples. In addition, the temperature raise on the sample surface was measured during glow discharge cleaning treatment and coating.

The optimisation goal was:

- a film thickness of 80 nm with a thickness uniformity of 5%
- a sputter rate of 5 nm/s at 80% of the mirror surface
- the best possible reflectance of the aluminium film in the wavelength range between 300 and 3000 nm.

Aluminium Film Reflectance

After coating in the VLT Coating Chamber, the reflectance of the samples was investigated in a reflectometer with an accuracy of about 0.1%. The reflectance measurement was absolute, not relative to a standard material whose reflectance must be known.

The reflectance data of the samples were compared (see Fig. 5) with two reflectance standards:

- The reflectance standard used in the USA: “Standard Reference Material 2003, Series E”, issued by the National Institute of Standards and Technology (NIST).
- “Infrared Reflectance of Aluminium Evaporated in Ultra-High Vacuum”, published by Bennet et al. in *J. Opt. Soc. Am.* 53, 1089 (1963).

Figure 5 shows the absolute reflectance versus the wavelength of the coated samples (solid line) in the ultraviolet, visible and infrared region. The circles (filled and not filled) represent the experimental points measured by Bennet (fresh and aged samples), while the asterisks represent the reflectance according to the US NIST standard.

Over the whole range from 300 to 2500 nm the results obtained in the VLT Coating Chamber are between the aged and not-aged Bennet data and are clearly above the NIST data.

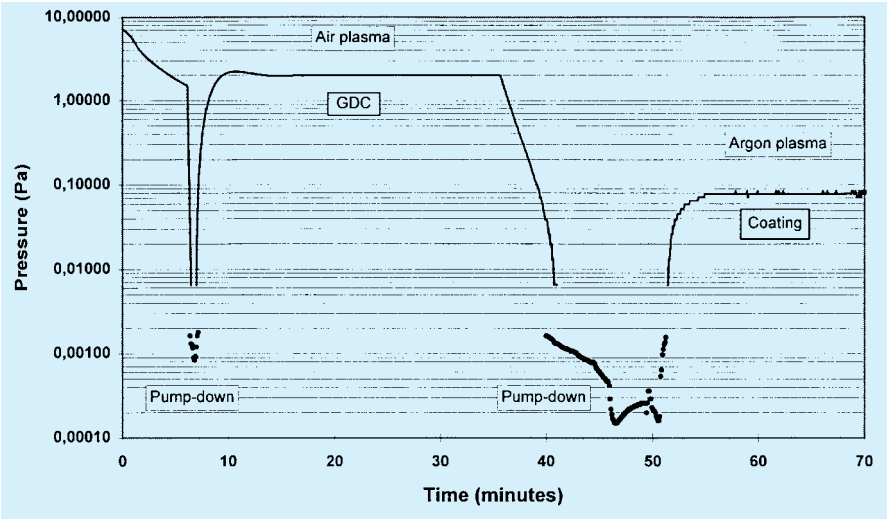

Figure 4: Chamber pressure during GDC- and coating process. After the GDC treatment, the high vacuum pump system pumps down the pressure inside the coating chamber (volume 122 m^3) from 2 Pa to 0.00015 Pa in less than 10 minutes.

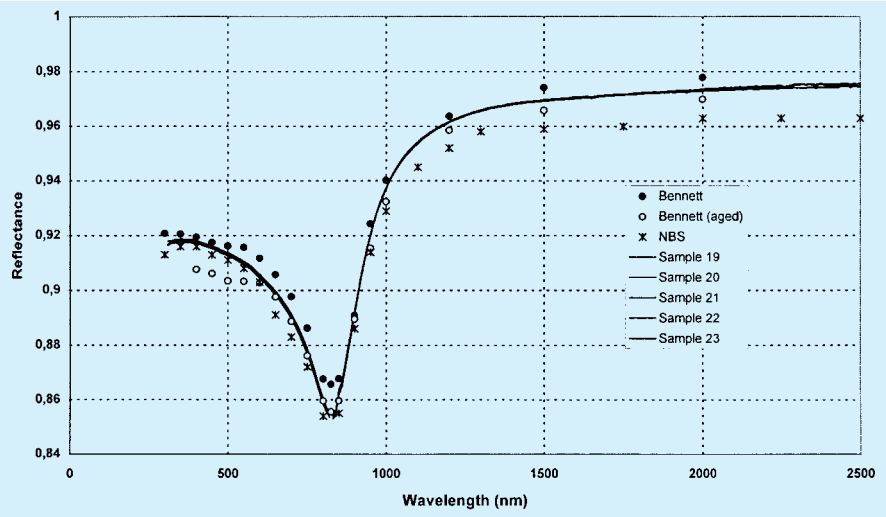

Figure 5: Measured reflectance values of coated samples (5 × 5 cm) as function of the wavelength in the range from 300 to 2500 nm (ultraviolet, visible, infrared). The results of the VLT Coating Unit are compared with the US standard NIST data and best possible measurements in a small laboratory system (Bennet et al. in J. Opt. Soc. Am. 53, 1089 (1963)).

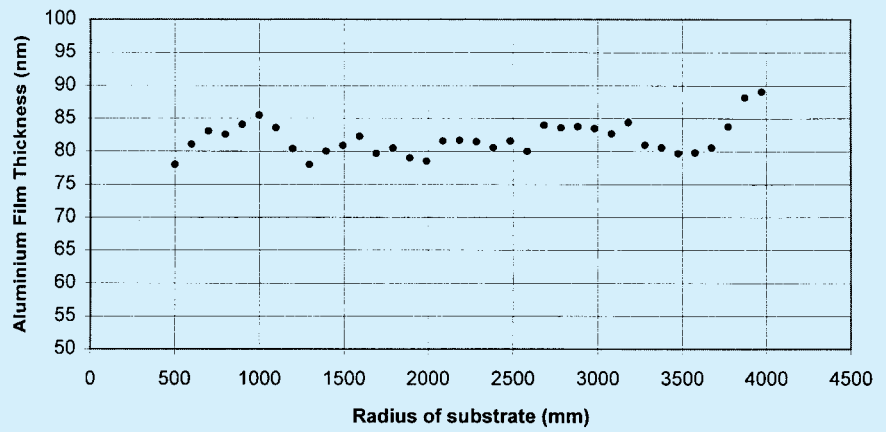

Figure 6: Aluminium film thickness, measured on glass samples along the radius of the mirror. Film thickness mean value 82.48 nm, standard deviation 4.16 % (3.43 nm).

Considering the size of the coating unit (chamber diameter more than 9 m, inner volume about 122 m^3) and the size of the mirror surface (more than 50 m^2) to be coated, the reflectance data measured are excellent.

Bennet's "ideal" data were obtained in a bakeable, grease-free, all-glass, small laboratory system. To reduce the possibility of oxidation of the aluminium during deposition, the evaporation was carried out in an ultra-high vacuum of about 10^{-8} Pa (vacuum inside VLT coating chamber 10^{-4} Pa prior to coating). During the measurement of the reflectance inside a reflectometer, the Bennet samples were flushed with dry nitrogen to minimise the rate of chemisorption of oxygen by the aluminium.

Due to these optimum test conditions Bennet's results are in very good agreement with the theoretically predicted reflectance data for highly pure (99.999%) aluminium and can be considered as the best possible experimental results.

Aluminium Film Thickness

Beside the reflectance, the film thickness of the sputtered aluminium was investigated.

With a special tool a line of coating was removed from the sample. The thickness of the step at the edge of this line was measured in at least three places with a profilometer.

Figure 6 shows the film thickness uniformity along the radius of the mirror (measured at single glass samples). At a mean film thickness of 82.48 nm the standard deviation was 4.16% (3.43 nm). This high film thickness uniformity over a radius of more than 4 metre shows the perfect adjustment of the trim shields and the shutter.

Depending on the magnetron discharge power, a dynamic deposition rate of more than 5 nm per second could be reached.

This rate is the film thickness divided by the time taken for a point on the mirror to cross the shutter opening. If the measured film thickness is δ nm and the mirror rotational speed is ω degrees per second, and the shutter opening is θ, then

$$\text{Rate} = (\delta * \omega)/\theta$$

Film Joint Zone

Special attention was given to the area where the film coverage was finished. The azimuth position of the joint line and the inclination angle with respect to the radius vector were exactly adjusted. The defined shutter control and the shadowing of the coating by the shutter edges resulted in a joint line zone, which could no longer be detected by variations in the film thickness uniformity. The only indication was a slight decrease in the reflectance (see Fig. 7) in the ultraviolet and visible region which could be measured in a band of less than 20 mm width. The reflectance in the infrared spectrum was not noticeably influenced.

Temperature Increase During Coating

In order to measure the temperature raise of the mirror during coating, thermocouples were glued to the bottom

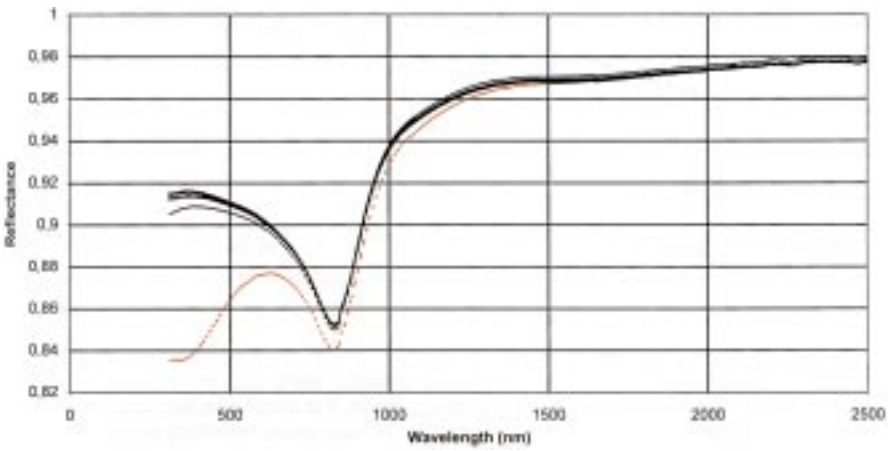

Figure 7: Decrease of reflectance in the ultraviolet and visible region of wavelength inside the joint line of the mirror at a radius of 2.1 m. The dotted lines show the beginning and the centre of the joint line zone, which had a width of less than 20 mm.

side of glass samples. Then they were positioned at 7 different radii and fixed thermally insulated onto the platform of the dummy substrate.

During the passages underneath the magnetron, the temperature increase on the samples could be determined at the same time when the aluminium film grew up.

The result was a temperature raise of less than 10°C on the surface. The samples at the outer radii warmed up more due to their larger clearance to the liquid nitrogen cooled shields underneath the shutter and the larger shutter opening.

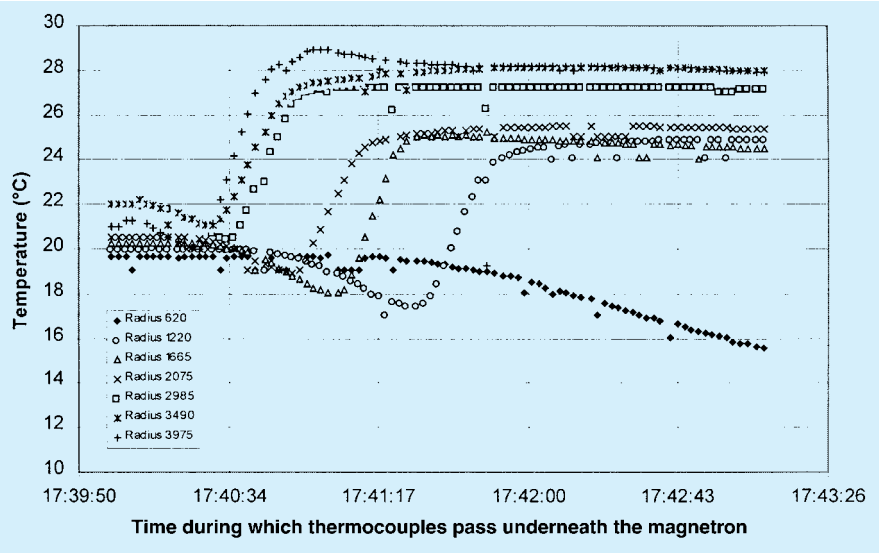

Figure 8: Temperature increase of the mirror surface during coating, measured by thermocouples positioned at 7 different radii and rotated underneath the magnetron. The magnetron discharge power was 102 kW, the rotation speed 20 degree per minute.

Summary

The sputtered aluminium film on the 8-metre-class mirrors produced in the VLT Coating Unit is very uniform along the whole radius (standard deviation 4.16%). The reflectance in the ultraviolet, visible and infrared regions is near to that which ideally can be expected. Furthermore, the dynamic deposition rate, defined as the film thickness cumulated in a single pass of the mirror past the source opening, is higher than 5 nm per second. The shutter system produces sharply stepped edges at the start- and end line of the coating and minimises the joint line to a width of less than 20 mm. All results are within or above ESO specification.

Climate Variability and Ground-Based Astronomy: The VLT Site Fights Against La Niña

M. SARAZIN and J. NAVARRETE, ESO

1. Introduction

Hopes were raised two years ago (*The Messenger* 89, September 1997) to be soon able to forecast observing conditions and thus efficiently adapt the scheduling of the observing blocks accordingly. Important steps toward this goal were achieved recently with the start of an operational service forecasting precipitable water vapour and cirrus (high altitude) cloud cover for both La Silla and Paranal observatories[1]. This was made possible thanks to the collaboration of the Executive Board of the European Centre for Medium Range Weather Forecasts (ECMWF) who accepted to distribute twice a day to ESO the Northern Chile output of the global model. The ground-level conditions[2] are also extracted from the ECMWF datasets with immediate benefits for observatory operation: bad weather warnings could be issued 72 hours in advance during the July snowfalls at La Silla. Once embedded into the Observatory control system, the temperature forecast is due to feed the control loop of the VLT enclosure air conditioning.

These forecast systems still have to be optimised and equipped with a proper user interface tailored to astronomer's expectancies. They might then join established celebrities like the DMD Database Ambient Server [3], paving the way to modernity for ground-based astronomical observing.

2. Unexpected, Improbable and Yet, Real

In this brave new world, however, not everything is perfect: as if the task of building a detailed knowledge of our sites was not hard enough, climatic events such as the El Niño–La Niña Oscillation (*The Messenger* No. 90, December 1997) can turn decade long databases into poorly representative samples. As was reported with UT1 Science Verification (*The Messenger* No. 93, September 1998), the VLT site started to behave anomalously in August 1998. A reanalysis of the long-term meteorological database pointed out an ever-increasing frequency of occurrence of bad seeing associated to a formerly quasi-inexistent NE wind direction. This contrasting behaviour is illustrated in the examples (Figs. 1 to 4) as displayed by the Database Ambient Server. While good seeing occurs under undisturbed NNW flow from above the Pacific, this NE wind is coming from land, it is rapid (Fig. 5), turbulent, and up to 2 degrees warmer than ambient. Finding its exact origin became a challenging task.

3. Searching for Clues

It is commonly stated that observatories are worse when operation starts than they appeared during the proceeding site survey. This is the well-known 3σ effect, the most outstanding site being probably at the top of its climatic cycle when it is chosen. This theory did not apply to the VLT site for which we had records since 1983 showing an impressive climatic stability. Therefore, before accusing *The Weather*, a complete investigation was undertaken, starting with man-made causes. In particular the chronology of the stresses imposed to the site since the construction of the VLT had started (e.g., water sewage, power generation, heat exchanging) were reviewed in collabo-

[1] http://www.eso.org/gen-fac/pubs/astclim/forecast/meteo/ERASMUS/

[2] http://www.eso.org/gen-fac/pubs/astclim/forecast/meteo/verification/

[3] http://archive.eso.org/asm/ambient-server/

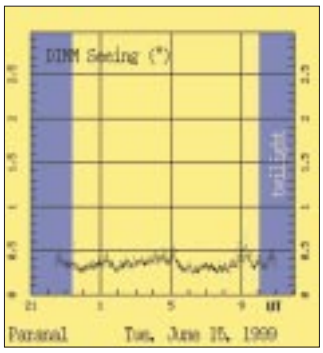

Figure 1: Seeing under standard Paranal NNW wind direction.

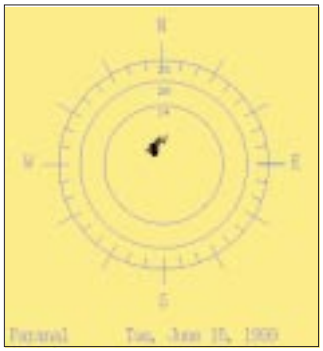

Figure 2: Standard Paranal NNW wind direction.

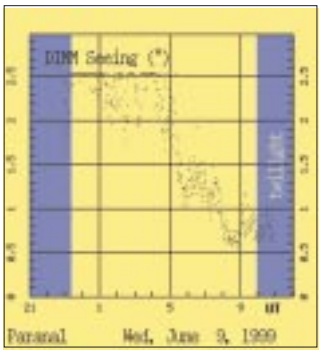

Figure 3: Seeing under infrequent Paranal NE wind direction (data are truncated for storage purposes.

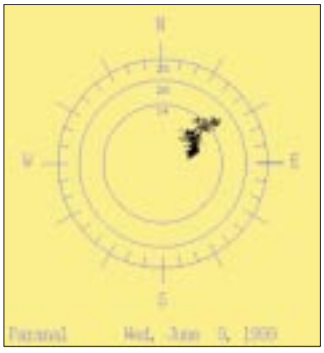

Figure 4: Infrequent Paranal NE wind direction.

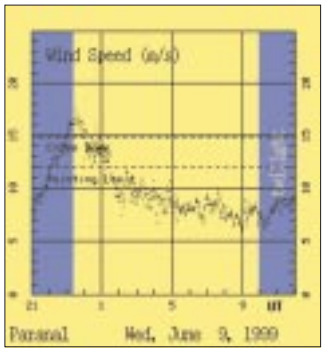

Figure 5: High wind velocities are typical with infrequent Paranal NE wind direction.

ration with the VLT staff at Paranal. This, completed by an infrared survey of the surroundings (Fig. 6), confirmed that man-made heat pollution was orders of magnitude smaller than the phenomenon we were witnessing.

Measurements of the turbulence in the ground layer of the telescope area were then conducted by the University of Nice[4]. The study results delivered in spring of 1999 revealed that the first 30 m above ground accounted for only 10% of the total. The turbulence borne by the NE wind was probably extending over one thousand metres or more up in the atmosphere and thus could not have been generated locally.

4. An Explanation in View

The inquiry turned then towards synoptic air motion but no obvious correlation could be observed between conditions at Paranal and the output of global models. The answer had to lie just in-between and the picture was slowly taking shape: if apparently stable condition like the good NNW Paranal wind were based on a fragile equilibrium of energy balance, a slight change in the global circulation could indeed induce noticeable modifications of the wind pattern in continental areas, locally tuned by the mesoscale orography. But, did such a change really occur?

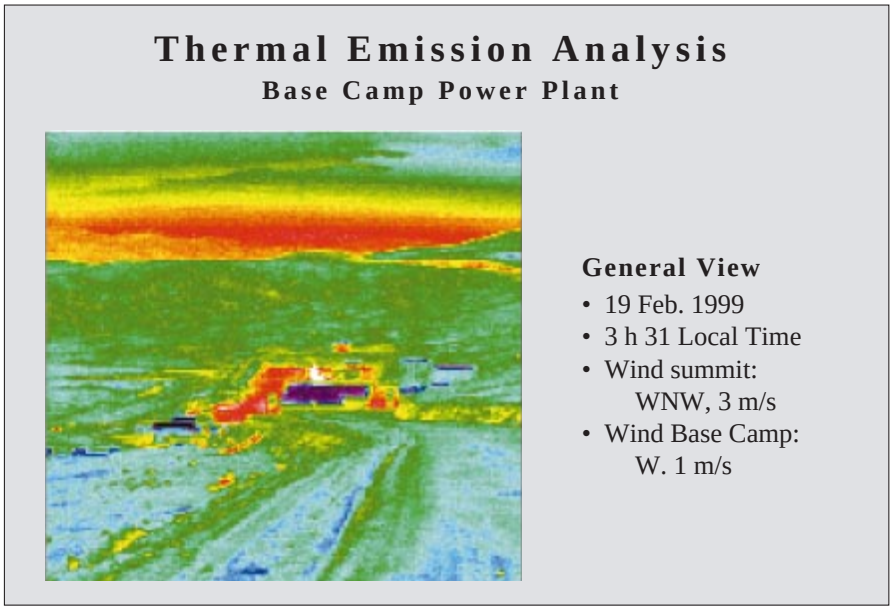

Figure 6: Thermal infrared night image of the VLT basecamp with the hot (white) powerplant plume in the centre. These heat sources are located several kilometres to the ESE on the lee side of the mountain. The thermally neutral access road is visible on the foreground.

It was then natural to ask the Chilean meteorologists who kindly and rapidly delivered the report reproduced herewith. This report stating that a weakening of the westerlies observed during the recent La Niña period constitutes the most plausible explanation to date. Indeed when compared to the last strong Niño event (1982–1984), the current slowly terminating oscillation has been fairly stronger in its Niña phase (Fig. 7), which coincides with the period of bad seeing at Paranal (July 1998 to April 1999).

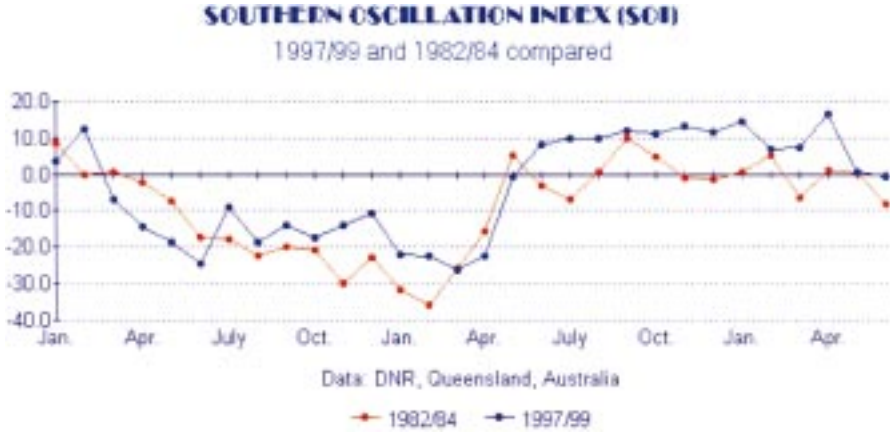

Figure 7: Comparison of the two strongest Niño events. A negative index corresponds to warmer waters (El Niño), a positive index to cooler (La Niña). The 1998–99 Niña period is stronger than the Niña of the previous cycle (1982–84) (http://www.vision.net.au/~daly/elnino.htm).

[4]Report on the GSM Measurement Campaign at the Paranal Observatory, Nov27–Dec20, 1998; F. Martin et al., Ref: VLT-TRE-UNI-17440-0006

Analysis of the Anomalous Atmospheric Circulation in Northern Chile During 1998

C. CASTILLO F. and L. SERRANO G., Department of Climatology of the Direction of Meteorology of Chile

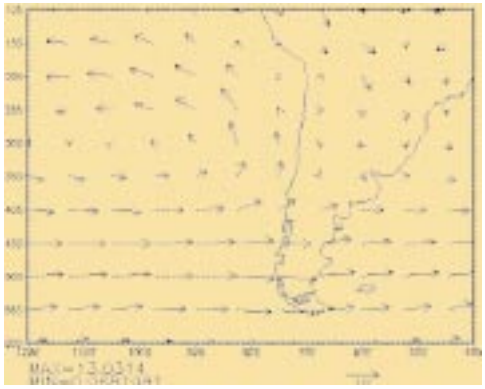

Figure 1: Circulation in 850 hPa.

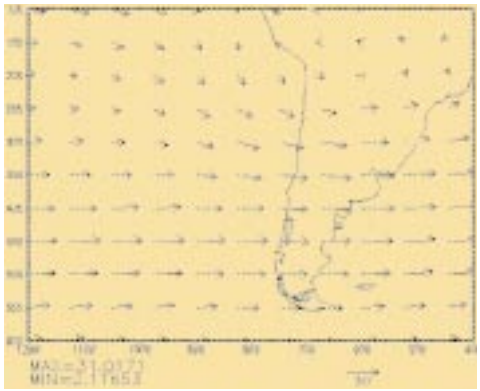

Figure 2: Circulation in 200 hPa.

In the far north of our country, wind components in the low and middle atmosphere until 700 hPa are normally from the North and from the East (Fig. 1), while above them and up to 100 hPa, West winds are normally prevailing during the whole year (Fig. 2).

It has been noticed that, during the years with La Niña or Antiniño occurrence, changes in the atmospheric circulation are of a global scale, similar to what is recorded during Niño years.

In Niña periods (as is the case since early 1998), the subtropical anticyclone of the South East Pacific which dominates the circulation in our country, becomes more intense and moves a few degrees southwards, resulting in a weakening of the high altitude (westerlies) winds over the far north of the country. To this adds the fact that the circulation on the eastern side of the Andes, which brings air from the Atlantic, becomes more intense from the low altitudes to the high atmosphere, up to the point at which the East component of the wind starts prevailing at high altitudes. This circulation pattern may be persistent enough to be seen on the Antofagasta radio soundings and is, as previously stated, directly related to La Niña events.

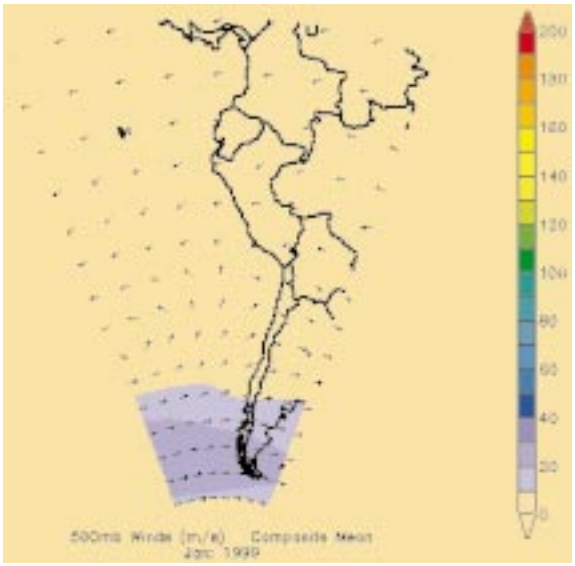

Figure 3: Circulation in 500 hPa (January 1999).

5. And What Comes Next?

Can we readily assume, looking at Figure 8 that Paranal is on its way to recover its original excellence? Hopefully yes, because although the average seeing still reflects some fairly bad events, the best 5 percentile were back into normal over the last two months, just as La Niña was vanishing . . .

6. Acknowledgements

We would like to thank Myrna Araneda Fuentes, Associate Director of the Department of Climatology of the Direction of Meteorology of Chile who provided the report reproduced herewith and José Vergara of the Department of Geophysics of the University of Chile for his helpful advice about mesoscale circulation.

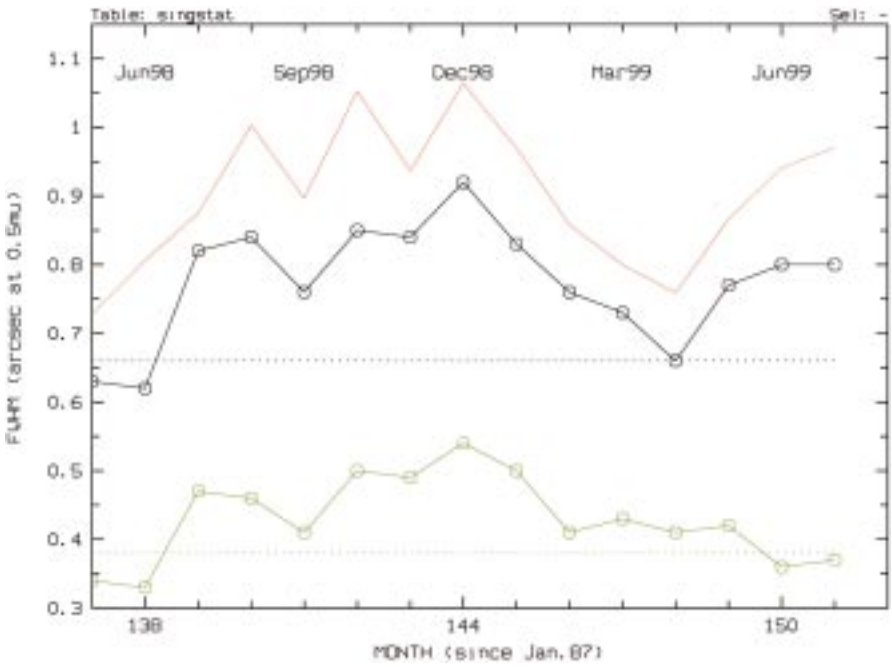

Figure 8: Seeing statistics at Paranal since UT1 first light: monthly average (red), median (black) and 5th percentile (green). The dashed lines give the respective long-term site characteristics. Seeing is reconstructed from DIMM measurements for an equivalent 20-min. exposure at 0.5 μm and at zenith.

Variable Curvature Mirrors

M. FERRARI, F. DERIE, ESO

Since the very beginning of the VLTI project, it has been foreseen that observations with this unique interferometer should not be limited to on-axis objects and the possibility to have a "wide" field of view (2 arcsec) was planned. It turned out that the "wide" field of view goal could not be achieved without a precise pupil management.

A variable-curvature mirror system (VCM), tertiary mirror of the delay line cat's eye, has been developed for this pupil management purpose. While the VLTI is tracking an astronomical object, the delay line provides for the equalisation of the optical path of the individual telescope by varying positions in the interferometric tunnel, and the VCM variable focal length permits positioning of the pupil image at a precise location after the delay line.

The range of radii of curvature required for the VCM is determined by the position of the delay lines. The two major parameters for the determination of this range are (1) the distance between the position of the pupil image following the coudé optics and the entrance of the cat's eye and (2) the distance between the exit of the cat's eye and the required position of the pupil image in the recombination laboratory. Considering the field of view planned for the VLTI (2 arcsec) and the OPD (optical path difference) to compensate for, the cat's eye secondary curvature must be continuously variable within a range from 84 mm^{-1} to 2800 mm^{-1} for the various configurations of 8-m Unit Telescopes and Auxiliary Telescopes.

Table 1: Required and achieved optical surface quality for the VCM.

• For radius 2800 mm:	
Required performance:	λ/4 PTV over ∅ 5 mm
Design Goal:	λ/10 RMS over ∅ 14 mm
Achieved performances:	λ/6.5 PTV over ∅ 5 mm λ/10.6 RMS over ∅ 14 mm
• For radii in the 230–2800 mm range:	
Required performance:	λ/2 PTV over ∅ 5 mm
Design Goal:	λ/2 PTV over ∅ 14 mm
Achieved performances:	λ/2.8 PTV over ∅ 5 mm
• For radii in the 84–230 mm range:	
Required performance:	3λ/4 PTV over ∅ 5 mm
Design Goal:	λ/2 PTV over ∅ 14 mm
Achieved performances:	λ/2.5 PTV over ∅ 5 mm

Realisation of the Mirror

The Optical Laboratory of Marseille Observatory (Laboratoire d'Optique de l'Observatoire de Marseille, LOOM) was selected for the design and realisation of this special device, because of its expertise in the active optics domain.

The location of the VCM in the delay-line system, on the piezo-translator used for small OPD compensation, led to minimise its weight and to realise a very small active mirror with a 16-mm diameter. The range of radii of curvature, with such a small optical aperture, corresponds to f ratio from plane to f/2.5, and the maximal central flexion achieved is 380 microns.

In the VCM system, presented with its mounting in Figure 1, the curvature is obtained with a uniform loading applied on the rear side of the mirror and produced by a pressure chamber. In order to use easily achievable pressure (<10 bar), the active part of the system is a very thin meniscus with a 300-micron central thickness.

Due to the large bending of the mirror, the full domain of curvature is not achievable with a classical optical material as vitroceramic glass (Zerodur). Metal alloys having 100 times higher flexibility than glasses, a stainless steel substrate (AISI 420) was chosen for the realisation.

Figure 1: Variable Curvature Mirror mounted and unmounted with its support. The active part is a very thin (300mm) meniscus and the deformation is achieved with a uniform air pressure applied to the back side of the mirror. The optical aperture is 16 mm.

Optical performances of the VCM

The VCM optical surface quality requirements were really tight for such an active mirror.

A careful analysis of the meniscus deformation, using theory of large amplitude elastic deformations, allowed to fulfil with success these requirements as presented in Table 1 and Figure 2.

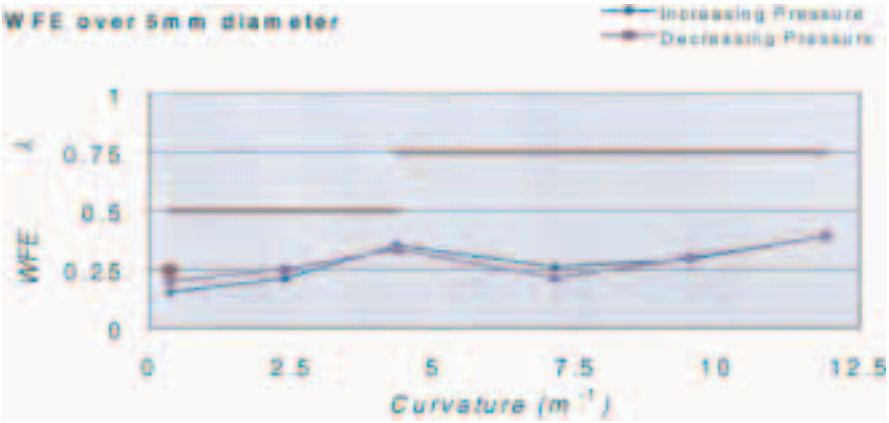

Figure 2: VCM optical surface quality over a 5-mm diameter. The wavefront error (WFE) is given as a peak-to-valley (PTV) in fraction of λ.

Figure 2 presents the optical quality (PTV) achieved with one of the VCM mirrors on the whole curvature range, compared to the required performances.

On the central part of the VCM, 5 mm diameter, analysis shows that the deviation from a sphere remains below λ/2 ptv during the whole curvature range (2800–84 mm).

Curvature Control Accuracy

The other important point, related to the pupil positioning in the interferometric laboratory, is the adjustment of a precise curvature during the operation of the VCMs.

In order to achieve a precise curvature, the air pressure on the back side of the mirror is controlled on open loop with a 5.10^{-4} accuracy in the 0–10 bar range. This high accuracy on the pressure control has been combined with an "hysteresis" model for the meniscus deformation. The effect is present only during the phase of decreasing pressure and depends on the maximum pressure reached during the cycle.

The model allows to take into account the history of the mirror and computes the right pressure to achieve the required curvature. An output of the model is presented in Figure 3 where ΔP is the correction to be applied (to correct for the hysteresis effect) as a function of the maximum pressure reached during the cycle.

Using the high-accuracy pressure control and the hysteresis model, the resulting error on the VCM curvature is less than 5.10^{-3} m^{-1} and leads to a 15-cm pupil position accuracy in the interferometric laboratory.

The error on the pupil position will be reduced by the beam compressor system, located at the entrance of the laboratory, to less than 1 cm at the instruments entrance and this value has to be compared with the 70 metres stroke of the delay line carriage.

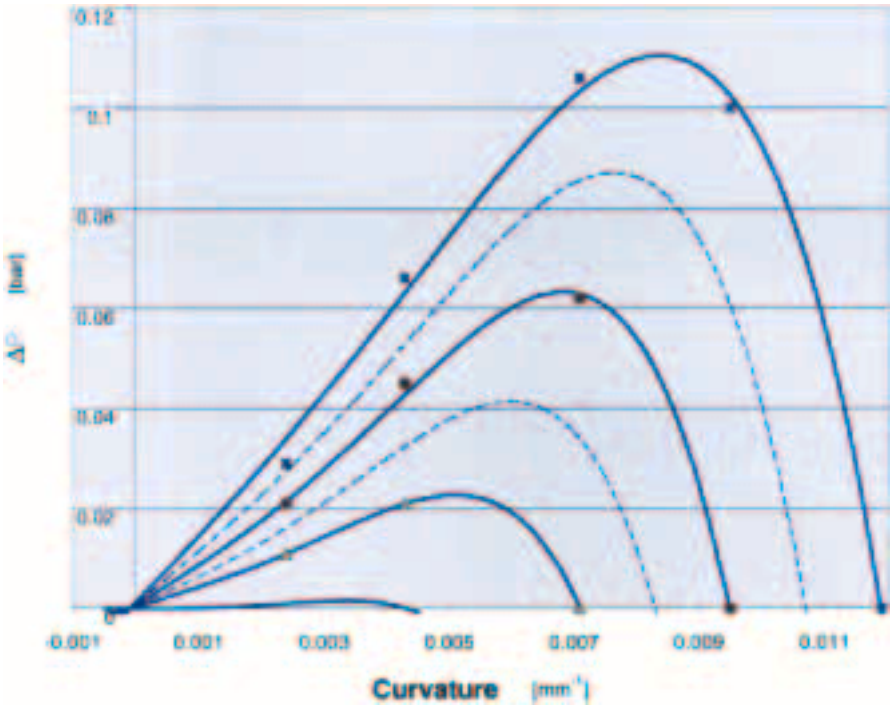

Figure 3: Correction to be applied to correct for the hysteresis effect. The lines represent the hysteresis model and the dots the measured values for various maximal pressures reached during a cycle.

Conclusion

This is not the first time that such an optical device, a varifocal mirror, has been achieved. But this one, thanks to the expertise of the team in Marseille Observatory, has an exceptionally wide range of curvature combined with a very good optical quality and a high curvature accuracy. This will allow the VLTI to deliver a good entrance pupil to the interferometric instruments.

Today this VCM has been delivered to ESO and is being included in the delay lines in order to set up and calibrate the interfaces with the other devices of the interferometric mode. The integration will be done during this year, the first complete systems (delay lines with VCMs) will be installed on Paranal during the year 2000.

The VLTI Test Siderostats Are Ready for First Light

F. DERIE, E. BRUNETTO and M. FERRARI, ESO

To allow the technical commissioning of the VLTI in its early phases, without the VLT Unit Telescopes or the Auxiliary Telescopes, two test siderostats have been developed to simulate the main functions and interfaces of these telescopes.

The principal objective of the optical concept (Fig. 1) of the siderostat is to optimise the collecting area over a sky coverage defined by the scientific targets chosen for the commissioning of the VLTI with the test instrument VINCI and the IR instrument MIDI. The diameter of the 400-mm free aperture of the Alt-Azimuth siderostat has been chosen to allow the observation in the N Band of all MIDI targets (Table 1). The angles between the different mirrors are optimised for the latitude of Paranal. To simulate the 80-mm diameter pupil size of a Unit Telescope,

Figure 1: Three-dimensional representation of the VLTI Test-Siderostat Optical Path. The diameter of the Siderostat mirror is 400 mm and the second plane mirror (upper part of the periscope) is at 25° angle of elevation. The use of a Beam Compressor allows to have an 80-mm output pupil (similar to the ones of the Unit Telescopes).

a beam compressor (5:1) is introduced between the Siderostat mirrors. The development of the beam compressor is made in collaboration with MPIA Heidelberg. The output pupil shape is, as expected by principle of a siderostat, an ellipse whose size and orientation vary in function of the direction of observation (Fig. 2). The small circle in the centre (at 0.0, 0.0 space Zenith position) represents the full aperture of the siderostat mirror. Field rotation due to Alt-Azimuth siderostat movement (bottom part of the figure) and vignetting due to the relay optics (central upper part) can be clearly identified.

Based not only on dedicated requirements for the optics, mechanics and control, but also on the above optical design and on the site interface, the development of two siderostats has been contracted to Halfmann Teleskoptechnik GmbH located at Neusäß near Augsburg. The detail design and the manufacture were achieved in less than one year. Figure 3, taken during the last assembly, shows the system ready for alignment tests prior to packing and delivery to Paranal. The five mirrors have an optical quality better than 25 nm RMS and are gold coated. The full structure is made of steel that preserves high rigidity. The dimensions are about 2.5 m in height and 2.2 m in diameter at the level of the yellow frame. Only the upper part will be visible above Paranal ground. The frame and the lower part will be located inside the AT station pier to have the output beam exactly at the level of the delay line entrance. With a weight of about 1.75 tons, the complete structure will be easily transported with a crane to allow, as requested during commissioning, relocation of the siderostat between AT stations. For this purpose a minimum of 8 stations will be equipped with a dedicated anchoring system.

Figure 3.

The functions of pointing and tracking are realised by a control system coupled to a CCD camera. The CCD is located at the focus of a guiding scope.

In the background of the picture one can see the two enclosures ready for packing. For these enclosures it was decided to re-use the same concept as for the Astronomical Seeing Monitor (ASM) that has been used for two years at Paranal. Taking advantage of the ASM experience, few modifications have been retrofitted to the design of the siderostat enclosure. What is not shown on the picture is the electrical cabinet that holds the control system. This cabinet will be located a few metres away from the enclosure.

Some performance tests have been carried out during the last weeks with good results. But, the fine-pointing per-

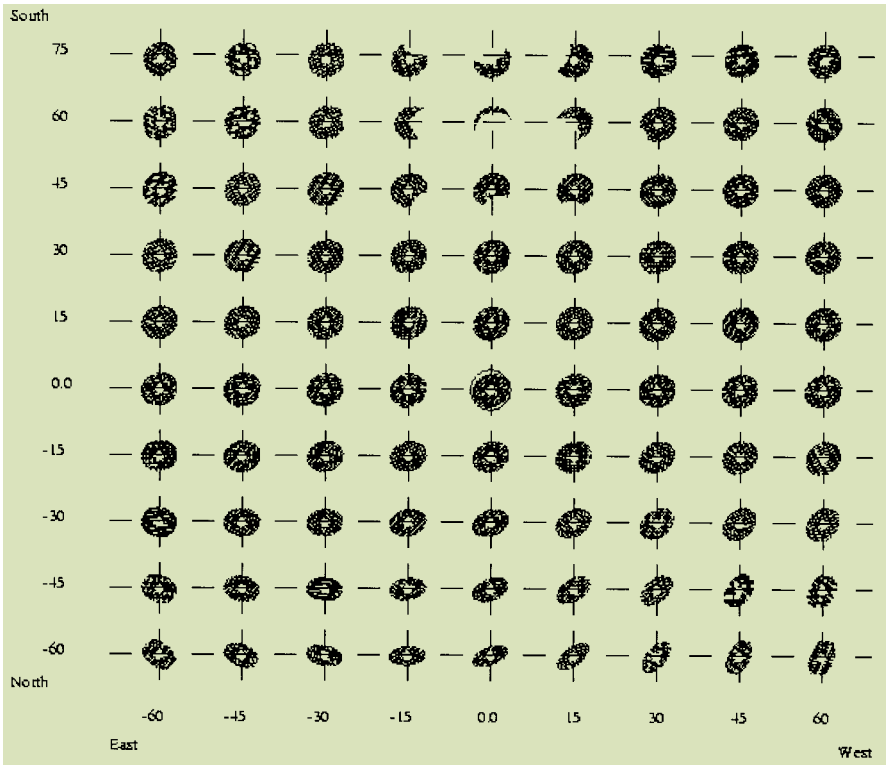

Figure 2.: Output pupil shape as a function of the direction of observation.

formance is still to be measured when good weather conditions will allow us to observe a star in the sky of Neusäß.

With an optical design optimised for the targets of the technical commissioning of the VLTI and its instruments, with high-quality optics, high rigidity of the mechanics and good control electronics, the two siderostats to be installed early 2000 will offer the capability to characterise the VLTI in its first phase. As done for the Astronomical Seeing Monitor, it is envisaged to upgrade the CCD camera by a VLT technical CCD and to perform the necessary upgrade of the control electronics and software to fully meet the ESO VLT standard.

Table 1: List of sources bright enough to be used with 400-mm diameter siderostats (C means N magnitude corresponding to correlated flux).

#	Object	1950 Coordinates	Magnitudes	
1	Alfa Ori	52 27.8 +07 23 58:	V=0.5	C=–4.5
2	Alfa Sco	26 17.9 –26 19 19:	V=1.0	C=–4.0
3	Alfa Tau	33 03.0 +16 24 30:	V=1.5	C=–3.0
4	L2 Pup	12 01.8 –44 33 17:	V=5.1	C=–3.0
5	R Leo	44 52.1 +11 39 41:	V=6.0	C=–3.0
6	IRC + 10 216	45 14.2 +13 30 40:		C=–3.0
7	V766 Cen	43 40.3 –62 20 25:	V=6.5	C=–3.0
8	Alfa Her	12 21.6 +14 26 46:	V=3.5	C=–3.0
9	VX Sgr	05 02.5 –22 13 56:		C=–3.2
10	R Aqr	41 14.1 –15 33 46:	V=6.4	C=–3.1

Myopic Deconvolution of Adaptive Optics Images

J.C. CHRISTOU[1], D. BONACCINI[2], N. AGEORGES[2], and F. MARCHIS[3]

[1]US Air Force Research Laboratory, Kirtland AFB, New Mexico, USA (christou@as.arizona.edu)
[2]ESO, Garching bei München, Germany (dbonacci@eso.org, nageorge@eso.org)
[3]ESO, Santiago, Chile (fmarchis@eso.org)

Abstract

Adaptive Optics produces diffraction-limited images, always leaving a residual uncorrected image and sometime PSF artifacts due, e.g., to the deformable mirror. Post-processing is in some cases necessary to complete the correction and fully restore the image. The results of applying a multi-frame iterative deconvolution algorithm to simulated and actual Adaptive Optics data are presented, showing examples of the application and demonstrating the usefulness of the technique in Adaptive Optics image post-processing. The advantage of the algorithm is that the frame-to-frame variability of the PSF is beneficial to its convergence, and the partial knowledge of the calibrated PSF during the observations is fully exploited for the convergence. The analysis considers the aspects of morphology, astrometry, photometry and the effect of noise in the images. Point sources and extended objects are considered.

1. Introduction

This paper reports on work done to establish and evaluate data reduction procedures specifically applicable to Adaptive Optics (AO) data. The programme evaluated for multi-frame iterative blind deconvolution, IDAC, is provided by J. Christou and available in the ESO Web page at `http://www.ls.eso.org/lasilla/Telescope/360cat/adonis/html/datared.html#distrib` for the Unix platforms.

This work is part of a dedicated effort to guide the AO users in the data reduction process and to produce specific data-reduction tools. The observing data presented here were taken with Adonis at the La Silla 3.6-m telescope during technical time, specifically dedicated to this data-reduction programme.

Adaptive Optics (AO) is now a proven technology for real-time compensation of space objects, to remove the degrading effects of the Earth's atmosphere. However, the compensation is never "perfect" and residual wavefront errors remain, which in some cases can lead to significant uncompensated power. This decreases the image contrast making, in some cases, necessary to use some form of image post-processing to remove the effects of the system's point spread function (PSF). The knowledge of good deconvolution techniques suitable on AO images is also important to boost images with low Strehl, e.g. from low-order AO systems.

AO compensation is achieved via a servo-control loop which uses a reference signal from a guide star (GS) to zero the wavefront error at each iteration, typically every 2–40 msec chosen depending on the observing wavelength and reference signal strength. It is well known that the performance of an AO system is limited by the reference signal strength as well as by the atmospheric coherence length r_0, the atmospheric coherence time to, and the isoplanatic angle θ_0.

In astronomical imaging, exposure times from a few msec to tens of minutes are used. The variability of r_0 and of the AO PSF can be quite large in short integration times (seconds), while it smoothes out in timescales of minutes. There is also a slow decline in Strehl Ratio (SR), the system's performance parameter[1], across an imaging field of radius θ_0 due to field anisoplanatism effect. The latter produces mainly an elongation of the PSF in the direction of the GS, which is function of the object radial distance. The PSF at the reference star has a diffraction-limited core, surrounded by a broad gaussian halo.

Static and dynamic artifacts in the image due to either print-through of the deformable mirror actuators, and differential aberrations between the science and WFS optical paths, have also been observed. For ADONIS, the former have a Gaussian shape with peak intensities in the range of 0.5% to 1% of the central PSF core. Although their energy content is undoubtedly small, if not removed they make it difficult to unambiguously identify faint objects or faint structures around bright sources.

Thus the observer has to worry about time-varying and space-varying AO PSFs.

In general, the observation of a point source as PSF Calibrator, in addition to the target, is used to further improve the compensated image via post-processing. However, the AO compensation obtained on the target and the PSF calibrator are not necessarily the same: the

[1]The Strehl Ratio is a standard measure for the performance of an AO system. It is the ratio of the maximum intensity of the delivered PSF to the maximum of the theoretical diffraction-limited PSF when both PSFs are normalised to unity. A Strehl Ratio of 1 means achievement of the theoretically best performance.

AO compensation depends upon the atmospheric statistics, i.e. the coherence length r_0 and the correlation time t_0, and how they relate to the sub-aperture size and sampling time of the AO system. These parameters vary in time between sets of observations of the target and the PSF calibrator, so that the AO system performs differently on each. In addition, the AO system is sensitive to the brightness and extent of the source used to close the loop. Both affect the signal-to-noise (SNR) on the wavefront sensor (WFS). In other words, the PSF calibrator obtained 'off-line' from the science observation does not give exactly the same PSF of the science frames, and the PSF is only approximately known.

So far, WFS using Avalanche Photodiodes (APD) in photon-counting mode have been used to rebuild the PSF from WFS data (J.P. Véran et al., 1997), obtained during the science acquisition. The method proves rather precise as long as the guide star is a point object and not too faint. Still, only an approximate PSF is recovered, especially with faint GS or with short exposure times.

Thus, in order to deconvolve the AO observations, it is useful to use an algorithm that is flexible with regard to the PSF as the latter is always known only with limited precision. A "blind" deconvolution algorithm is very suitable for this application. We call it 'myopic' as the AO PSF is rather well known, although not perfectly, either via the PSF calibrator method or via the PSF reconstruction from WFS data.

We report here on the iterative 'myopic' deconvolution technique, which takes advantage of multiple frames taken under variable PSF conditions. Starting from an approximately known average PSF, and assuming that the science object is constant in time, the algorithm runs relaxing the PSF in each frame and finding the best combination of PSFs which deliver the common science object in all the frames. The input is an approximated average PSF and a set of N science frames taken with the same instrumental set-up. The output is the science object recovered, and a set of N PSFs. In general, the more the PSF varies between frames, the easier the science object detection is. As it is known that the PSF in closed loop varies in time scales of seconds, this myopic iterative deconvolution algorithm is very well suited to AO data. Long-exposure images taken in different seeing conditions, e.g. with different PSFs, also benefit from this deconvolution method.

Deconvolution algorithms use a "known" PSF to deconvolve the measurement. This is classically an ill-posed inverse problem which has been well studied in recent years, and algorithms such as Lucy-Richardson are readily available (Lucy, 1974). Multiframe iterative blind deconvolution (IBD), which solves for both the object and PSF simultaneously, is ill-posed as well and also poorly determined. However, the application of physical constraints upon this algorithm permits both the object and PSF to be recovered to an accuracy that depends mainly upon the SNR of the observations (Sheppard et al., 1998).

We discuss the physically constrained iterative deconvolution algorithm, described in section 2, and its application to both simulated and real data sets described in sections 3 and 4. The simulations permit us to investigate the algorithm's performance given a known target. We briefly show the effect of noise on photometry, astrometry and morphology. Different data types are investigated including multiple point source targets, binary stars, a galaxy image, Io and RAqr for different SNR conditions. This permits performance evaluations on real data sets by comparison to the predictions of the simulations. As previously mentioned, the algorithm also recovers the PSFs for the observations, and investigation of these permit evaluation of the AO system's performance e.g. on non-point-like targets.

We are assuming that the PSF is constant across the processed field of view, i.e. we neglect anisoplanatism effects. Work on the latter is in progress at ESO in collaboration with the Osservatorio Astronomico di Bologna, and it will be reported later.

2. The Algorithm

The IDAC code is based on the conjugate gradient error-metric minimisation, blind deconvolution algorithm of Jefferies and Christou (1993) and is currently under further development and testing by an extended group. The advantage of multiple frames is to have more information to break the symmetry of the problem. For a single frame, the target and PSF are exchangeable without using prior information. For multiple frames, a common object solution is computed along with the corresponding PSF for each observation in the data set. Note that PSF static artifacts in the image will be considered part of the object, and have to be calibrated out. This is done in several ways, e.g. processing the PSF calibrator data with this same code, extracting the static components and removing them from the science object at the end of the processing, or using images of an artificial point source on the AO setup.

The standard isoplanatic imaging equation can be written as

$$g'(\vec{r}) = f(\vec{r}) * h(\vec{r}) + n(\vec{r}) \quad (1)$$

or in the Fourier domain as

$$G'(\vec{f}) = F(\vec{f}) \cdot H(\vec{f}) + N(\vec{f}) \quad (2)$$

where $g'(\vec{r})$ is the measurement, $f(\vec{r})$ is the target, $h(\vec{r})$ is the blur or PSF of the system and * denotes convolution. $n(\vec{r})$ represents noise contamination which can be some combination of photon noise and detector noise. The Fourier transforms are indicated by the corresponding uppercase notation, where $\vec{r}$ is the spatial index and $\vec{f}$ is the spatial frequency index.

For the blind deconvolution case, both the target and PSF are unknown quantities. In order to solve for these we apply an error-metric minimisation scheme using a conjugate gradient algorithm simultaneously minimising on several error-metric terms. The first is known as the fidelity term which measures the consistency between the measurements and the estimates.

$$E_{\mathrm{F}} = \sum_k \sum_{i \in R} | g'_{ik} - \hat{f}_i * \hat{h}_{ik} | \cdot s_{ik} \quad (3)$$

where k is the frame index and i is the pixel index and s_{ik} is a "bad" pixel mask which eliminates cosmic-ray events and "hot" and "dead" pixels from the summation. The $\hat{}$ indicates the current estimates of the variables.

One of the problems with many of these iterative algorithms is knowing when to terminate the iterations. From (1) and (3) it can be seen that when an exact solution is reached, the error-metric does not go to zero but to a noise bias, i.e.

$$\begin{aligned} E_{\mathrm{F}} &= \sum_k \sum_i | g'_{ik} - \hat{g}_{ik} | \cdot s_{ik} \\ &= \sum_k \sum_i | n_{ik} | \cdot s_{ik} = KN\sigma_N^2 \end{aligned} \quad (4)$$

where zero-mean Gaussian noise of rms σ_N has been assumed for K frames and N pixels per frame. Thus, truncating the iterations at this limit is consistent with the noise statistics and is an effective regularisation procedure to minimise "noise amplification error".

It is also necessary to apply physical constraints to both the object and PSF. Both are positive and following the approach of Thiébaut & Conan (1994), we reparameterise both as square quantities, i.e.

$$\hat{f}_i = \phi_i^2 \qquad \text{and} \qquad \hat{g}_{ik} = \varphi_{ik}^2 \quad (5)$$

It is also noted that the PSF is a band-limited function due to the physical nature of the imaging system, i.e. the telescope used has a finite aperture and therefore the PSF has a finite upper-bound to its spatial frequency range $f_c = \Delta/\lambda$. Thus the PSF estimate is penalised for containing information beyond this spatial frequency limit by the following error metric,

$$E_{\mathrm{BL}} = \sum_k \sum_{u \in U} H_{uk} \quad \text{for} \quad u > f_c \quad (6)$$

2.1 Myopic deconvolution

Prior PSF information is utilised reducing the PSF parameter space, better avoiding local minima solutions, and also helping to break the symmetry. This is applied in the form of a mean PSF for the multiple-observation data set. In order to remove the effects of mis-registration from one frame to another, the shift-and-add (SAA) or peak-stacked mean of the PSF estimates is computed,

$$\hat{(h_i)}_{\mathrm{SAA}} = \sum_k \hat{h}_{k(i-i_{\mathrm{pk}})} \qquad (7)$$

where i_{pk} is the intensity peak location of the k^{th} frame. The SAA image is then compared to the SAA image of a reference star by using the following error-metric,

$$E_{\mathrm{SAA}} = \sum_k \left[(h_i)_{\mathrm{SAA}} - \hat{(h_i)}_{\mathrm{SAA}}\right]^2 \qquad (8)$$

Equation 3 computes the fidelity term in the image domain. The advantage of this is to permit the application of support constraints to the measurement as well as bad-pixel masks. However, Jefferies & Christou (1993) originally computed EF in the Fourier domain where there is the advantage of applying a bandpass-limit to the observations, i.e. so that those pixels in the Fourier domain which lie outside the cut-off frequency f_{c} are excluded from the summation. A modification to this is to apply a spatial frequency SNR weighting for those spatial frequencies which lie within the cut-off frequency, i.e.

$$E_{\mathrm{F}} = \sum_k \sum_{u \in U} \left| G'_{uk} - \hat{F}_u \cdot \hat{H}_{uk} \right| \cdot \Theta_{uk} \qquad (9)$$

where Θ_{uk} in the simplistic case is simply a band-pass filter, i.e. is unity for spatial frequencies lower than f_{c} and zero outside. However, it can also be defined as a low-pass filter customised to the SNR of the data, e.g. an Optimal Filter (in the linear minimum mean squared error sense.)

$$\Theta_{uk} \approx \frac{|G'_{uk}|^2 - |N_{uk}|^2}{|G'_{uk}|^2} \qquad (10)$$

where $|N_{uk}|^2$ is assumed to be white noise and is obtained from the mean value of $|G'_{uk}|^2$ at spatial frequencies > f_{c}.

The algorithm minimises on the combined error metric of the individual ones described above, i.e.

$$E = E_{\mathrm{F}} + \sum_j \alpha_j E_j \qquad (11)$$

where α_j are weights which regularise each of the additional error-metric terms.

3. Application to Simulated Data

In order to demonstrate the algorithm's performance on AO data, during our study it was first applied to simulations. In this section we present results from application to a simple object – a set of multiple point sources for which the astrometry and photometry can be recovered. The algorithm is next applied to a far more complicated target, a galaxy.

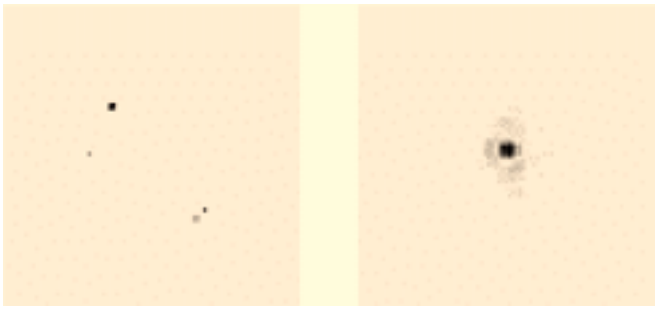

Figure 1 Left: simulated multiple-point source truth (4 sources). Note that each star is centred on a single pixel. Right: sample PSF from the data cube. Note the diffraction-limited core and Airy rings broken up by residual aberrations. (Both images displayed on a square root scale.)

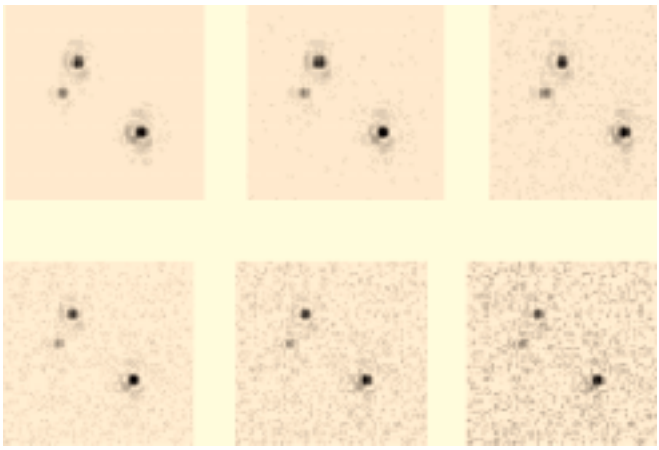

Figure 2: First frame of the data set for the six different SNR cases with the noise increasing from left to right and top to bottom. (All images displayed on a square root scale.)

3.1. Multiple-Star Case

A data set comprised of four point sources was created and convolved with a data cube (64 frames) of simulated atmospheric PSFs for D/r_0 = 2 such that each of the PSFs was dominated by a diffraction-limited core but there was also speckle noise. Figure 1 shows the "truth" object and one of the "truth" PSFs. Six different levels of zero-mean Gaussian noise then contaminated these simulated data. Table 1 gives the SNR levels (or dynamic range) for these cases as defined by the ratio of the peak signal in the data cube to the rms of the noise (PSNR). Figure 2 shows the first frame of the data cube for the six different SNR cases.

For the initial tests, all 64 frames of the data cubes were reduced simultaneously. The algorithm was minimised on the fidelity term (computed in the image domain) and the bandpass constraint only, $E = E_{\mathrm{F}} + E_{\mathrm{BL}}$, using the SAA image of the measurements as the initial object estimate (see Fig. 3) and the SAA image of the brightest source was used as the initial PSF estimate. Note that this source is in fact a close binary. Thus, the algorithm was not run "blind" but reasonable starting "guesses" or estimates were used based on the data. The iterations were terminated when either the noise limit (equation 4) was reached or when the error-metric changed by less than one part in 10^6.

The resulting reconstructed objects are shown in Figure 4. In all six cases. All four sources have been recovered, and in nearly all cases, the individual sources are restored to a single pixel demonstrating the algorithm's ability to "super-resolve". Comparison of the lowest SNR case reconstruction clearly shows detection of the faintest source which is very ambiguous and masked by noise in the raw data (Fig. 2). Comparison to the SAA images (Fig. 3) shows the faintest source to be a "brightening" of the Airy ring around the brightest object. The super-

PSNR (P)	DB [20 $\log_{10}$(P)]	Δ Magnitude
819	58	7.3
410	52	6.5
205	46	5.8
102	40	5.0
51	34	4.2
26	28	3.5

Table 1: Signal-to-noise ratios for the simulated multiple-star data sets given as the ratio of the peak signal to the rms of the additive noise (PSNR) as well as in decibels and stellar magnitudes.

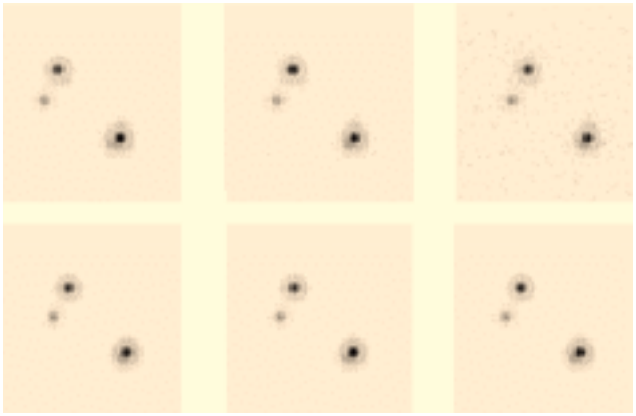

Figure 3: Initial object estimates for the six different SNR cases with the noise increasing from left to right and top to bottom. Note that the brightest source (bottom left) was used as the initial PSF estimate. (All images displayed on a square root scale.)

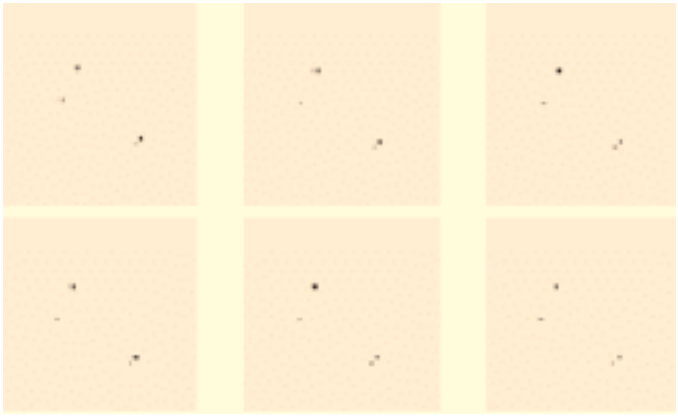

Figure 4: Reconstructed objects for the six different SNR cases with the noise increasing from left to right and top to bottom. (All images displayed on a square root scale.)

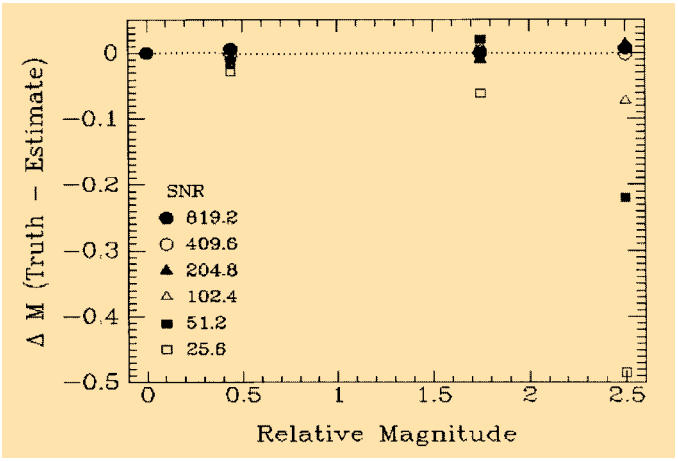

Figure 5: Residual photometry errors from measuring the brightest pixel for the four sources in the object reconstructions for the 6 different SNR cases compared to the sources' true brightness normalised to the brightest source.

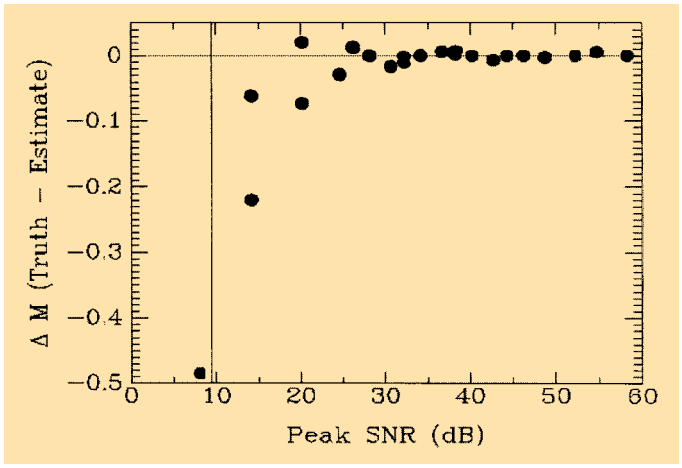

Figure 6: Residual photometry errors of Figure 5 plotted against the SNR of the 4 sources for the different SNR conditions. The horizontal dashed line represents perfect reconstruction and the vertical dashed line represents the 3σ noise level.

resolution of the algorithm permits it to be detected as a separate source.

Using multiple point-source objects makes it relatively easy to determine the reconstructed object fidelity permitting direct measurements of not only the astrometry, i.e. the relative positions of the sources, but also the relative photometry, i.e. the brightness of the sources. In all cases, the relative locations of the sources matches the truth. The relative photometry was computed, in stellar magnitudes, by measuring the peak pixel values of the four sources since the sources were all initially located at integer pixel locations. Figure 5 shows the residuals of the photometry as a function of the sources' true brightness values. Note that as the SNR decreases, the fidelity on the fainter source becomes worse in a systematic way with the magnitude difference increasing as the noise.

The reason for the underestimation of the fainter sources is because of the presence of the noise. This is further illustrated in Figure 6. This plots the residuals from Figure 5 against the SNR of each of the four sources for the six different SNR con-

Figure 7: Reconstructed PSFs for (left to right) decreasing SNR for the first frame of the data cube. ***Top:*** *the brightest source used as the initial PSF estimate. Note its contamination by the faintest source.* ***Bottom:*** *reconstructed PSFs.* ▼

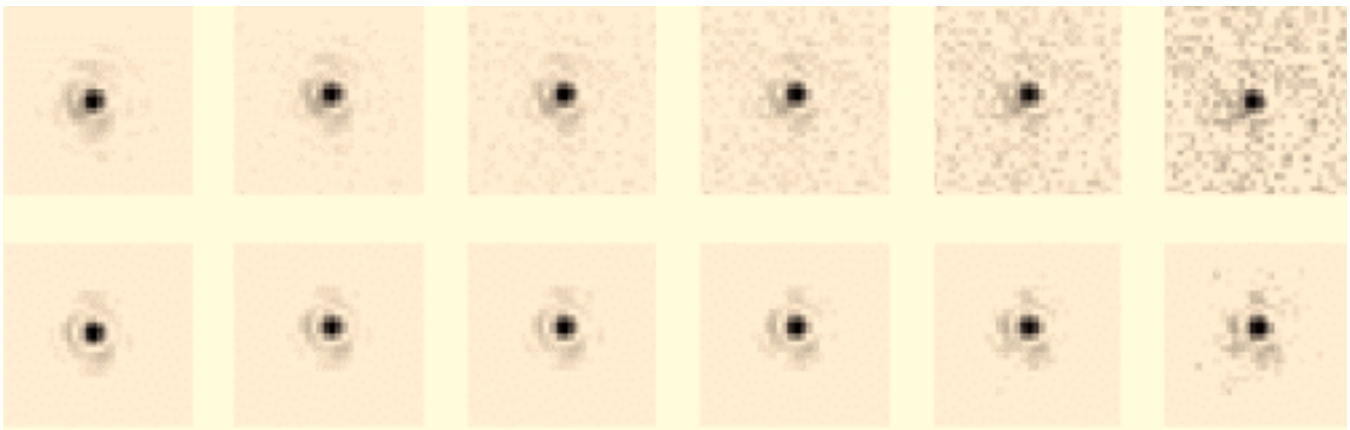

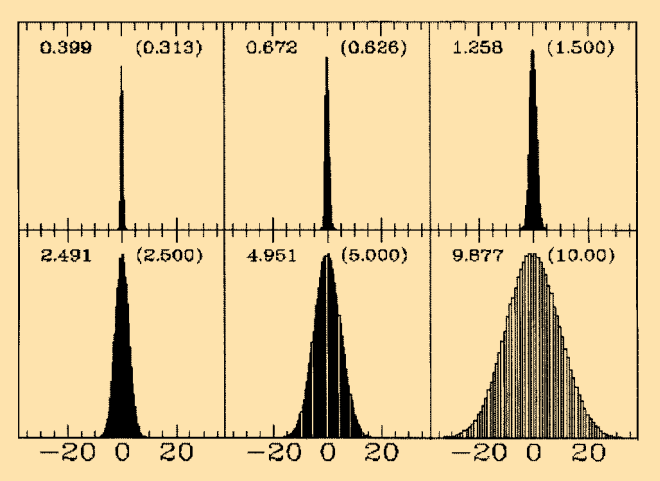

Figure 8: Histograms of the residuals for the six different SNR cases. The measured residuals rms value is shown for each case compared to the rms value of the input additive noise (in parentheses).

ditions. Note that the poorest reconstruction is below the 3σ level and that good reconstructions are obtained for SNRs greater than 6σ. This demonstrates that the sources that become "lost" in the noise are difficult to extract accurately.

As mentioned above, the object and the PSF are both reconstructed using deconvolution. Figure 7 shows the reconstructed PSF for the first data frame of the data cube for each of the SNR cases compared to the initial estimates for the first frame of the data cube. Comparison of the highest SNR case shows good agreement between the reconstruction and the "truth". As the SNR decreases, there is little difference in the reconstructions with more noise for the lowest SNR case. This analysis is useful when planning the observation's integration times, according to the desired photometric accuracy.

3.1.1 Effect of noise propagation

We ask "How well does the algorithm deal with the noise?" As seen above, some noise does appear in the object reconstructions and the PSFs, especially for the higher noise cases, but most of it shows up in the residuals. This is illustrated in Figure 8 which shows histograms of the residuals for the 6 different SNR reconstructions. As can be seen, these histograms appear to have Gaussian distributions. The rms value of the residuals compare very favourably to the input noise statistics and the residuals do have a zero-mean. The reduced photometric accuracy for the lower SNR cases shows the effect of the presence of noise on the algorithm's ability to break the symmetry between the PSF and the object, especially when using initial noisy PSF and object estimates.

These results demonstrate the algorithm's ability to recover not only the object distribution but also the corresponding PSFs for different SNR conditions. The residuals compare well to the input noise conditions, and relative photometry of the reconstructed object shows results consistent with the different SNRs. In all cases, 64 frames were reduced. For these data, the PSFs have a common diffraction-limited core but have different speckle noise. Thus, the multiple frames are significantly different from each other.

3.1.2 Effect of frame multiplicity

The next question we ask is "How well does the algorithm perform as the number of frames is reduced?" This was investigated by taking the third highest SNR data and reducing it using 1 set of 64 frames, 2 sets of 32 frames, 4 sets of 16 frames, 8 sets of 8 frames and 16 sets of 4 frames. The reconstructed object for the first of each of these sets is shown in Figure 9. Note that there appears to be little difference between them. The relative photometry of the four sources was calculated from the peak pixel values as above for all reconstructions. The mean and standard deviations were computed for the multiple reduction cases, i.e. when the number of frames was less than 64, and these are shown plotted in Figure 10. This shows the repeatability of the photometry and indicates that when the number of frames used is relatively small, i.e. ~ 8 or less, then the photometry on the fainter sources can show significant variation. There is also a trend that as the frame number decreases, the photometry of the fainter sources is underestimated. This is probably indicative of the combination of high noise and small number of frames making it difficult for the algorithm to distinguish between signal and noise.

3.2 Galaxy case

The multiple star represents imaging of a relatively simple object. A more typical extended target is that of a galaxy. Two sets of AO observations of a barely resolved galaxy were generated. The first using simulated AO PSFs for good compensation with SRs of ~ 50% which is typical of that expected by using e.g. a 60-element curvature system in K-band. The second had a much poorer compensation with SRs ~ 10% typical of a faint GS. The former data set were computed from simulated PSFs, whereas the latter was obtained from ADONIS observations of a faint isolated star. Each PSF data set comprised ten separate frames. These PSFs were over Nyquist sampled by a factor of two corresponding to an image scale of 32 mas/pixel assuming K-band imaging on a 3.6-m telescope.

The galaxy reference image for the simulations was obtained from the 512×512 galaxy image contained in the IRAF system. This was reduced using 8×8 pixel block sums to a 64×64 pixel image which was then embedded in a 128×128 pixel field. This image was then convolved with the PSFs and then contaminated by zero-mean additive noise with PSNRs of 1000, 200 and 50 corresponding to dynamic ranges of 7.5, 5.8 and 4.2 magni-

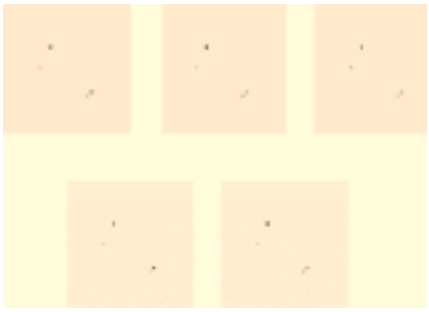

Figure 9: Reconstructed object for the third highest SNR case for (left to right and top to bottom) 4, 8, 16, 32, and 64 frame reductions.

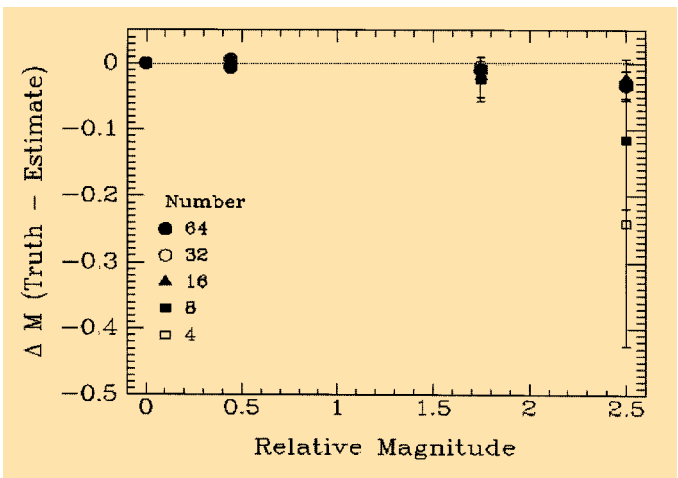

Figure 10: Residual photometry errors from measuring the brightest pixel for each of the four sources in the object reconstructions for the different multiple-frame reductions. The mean and standard deviations are shown for the reductions using less than 64 frames.

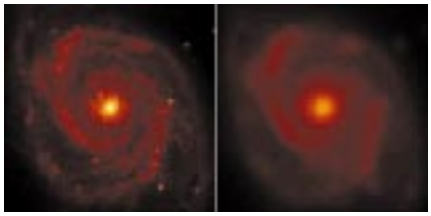

Figure 11: Simulated AO galaxy observations for high SR (left) and low SR (right). (Displayed on a square-root scale intensity.)

tudes respectively. Figure 11 shows the uncontaminated mean observation for the two SNR cases obtained from shift-and-add analysis.

Figure 12 illustrates the effect of the additive noise on the resolution of the images. The complete average power spectrum of the ten frames for the 3 SNR cases of the lower SR data radial profiles are shown. Also shown are the noise bias levels. Where they intersect with the data spectrum is more clearly seen in the top panel which shows the SNR of the measured power spectrum. Note that the highest spatial-frequency passed by the pupil is set to unity and for a PSNR of 1000, this is reached. However, as the noise increases, the effective frequency cut-off decreases to 0.85 for a PSNR of 200 and to 0.52 for a PSNR of 50. Thus, high spatial frequency information is further corrupted by the additive noise.

The data sets were reduced using the noisy SAA image as the initial object estimate and a SAA of a reference star as the initial PSF. This PSF estimate was obtained from the same set of data, which created the galaxy images, but excluding the used PSFs. The iterations were terminated when the noise bias level was reached. Full-field support was used for the object and the PSFs as well as the band-limit. All six cases have been analysed (3 SNRs each for the two SR cases). For both SR cases, it can be seen in the curves of Figure 13 that as the SNR decreases, the effective resolution also decreases. Also, the higher the initial SR, the better the reconstruction. Super-resolution is achieved over the diffraction-limited image for all but the lowest SNR case for the lower Strehl data, which is restored to diffraction-limited. The reconstructions show the detectability of the spiral arm structure lost in the raw compensated images.

Figure 13 shows the radial profiles of the Fourier moduli of the low SR reconstructed images compared to the truth (the top line of the four). The vertical lines indicate the noise-effective cut-off frequency f_N (see Fig. 12) for the three SNRs. These plots show that within f_N, there is good reconstruction but for the super-resolution regime, in these cases for $f > f_N$, the higher spatial frequencies are attenuated with respect to the truth. In order to quantitatively measure how good the reconstruction is, the normalised cross-spectrum was computed between the reconstruction and the truth, i.e.

$$XS_i = \frac{|F_i \cdot \hat{F}_i^*|}{F_i \cdot F_i^*} \qquad (12)$$

which will be unity for a perfect correlation. Note that the numerator is the modulus of the cross-spectrum only so that mis-registration of the two images does not affect the value. The summation of XS_i, yields the correlation coefficient for the reconstruction, i.e.

$$\gamma_\Lambda = \sum_{i \in \Lambda} XS_i \qquad (13)$$

where Λ represents the spatial frequency region over which the summation is computed. Setting Λ to the SNR support (see Figure 12) yields correlation coefficients of 1.1, 1.0 and 0.9 for decreasing signal-to-noise showing excellent reconstruction within those regimes.

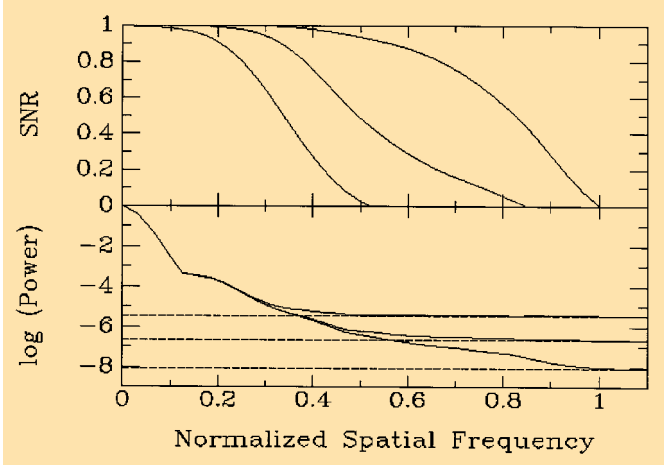

Figure 12: How noise affects resolution. The bottom panel shows azimuthally averaged power spectra for the three SNR observations of the lower SR data. The top panel shows the corresponding SNR. Note that as the noise increases the cut-off frequency decreases.

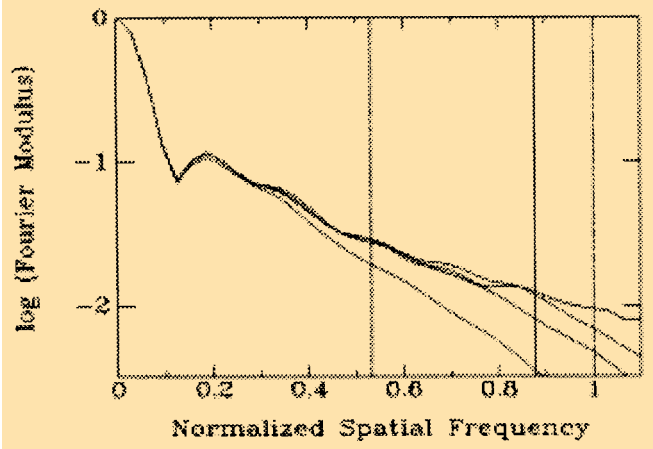

Figure 13: Azimuthally averaged radial profiles of the Fourier moduli of the reconstructed images for the lower SR data. Decreasing SNR gives lower spatial frequency cutoff and worse MTF.

4. Application to ADONIS Data

In this section, we present results of the IDAC algorithm as applied to different types of measured data. This includes binary stars, then the Galilean satellite Io as an extended object, and R Aqr, which has faint structure around a bright central source.

4.1. Closeby point sources: τ Canis Majoris

Data were taken of the bright binary star τ CMa (= HR2782 = ADS 5977A) at the ESO 3.6-m during a technical run in February 1996. The Yale Bright Star Catalogue lists it as being an O91b star of m_v = 4.40, having an equal magnitude companion at a separation of 0.2″. More recently, the CHARA group have measured it obtaining a separation of 0.160″ in 1989.9 (Hartkopf et al., 1993). The diffraction-limits of the telescope are 0.072″ at J (1.25μm), 0.095″ at H (1.65μm) and 0.126″ at K (2.2μm). Thus the data were Nyquist-sampled at J, i.e. at 0.035″/pix-

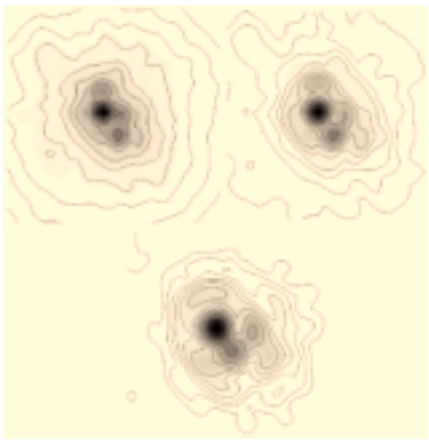

Figure 14: J (top left), H (top right), and K-band (bottom) peak tracked images (smoothed to remove the pixel-to-pixel variations) with superimposed logarithmic contours emphasising the extended halo structure in the images. The contour levels are at 1, 1.6, 2.5, 4, 6.3, 10, 16, 25, 40, 63% of the peak value in each of the images.

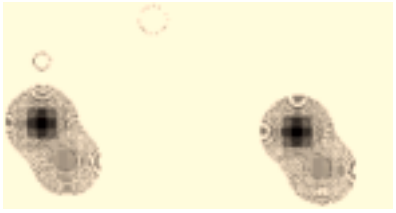

Figure 15: J-band τ CMa object reconstructions for the first (left) and second (right) 16 frames. Same contour levels as Figure 14.

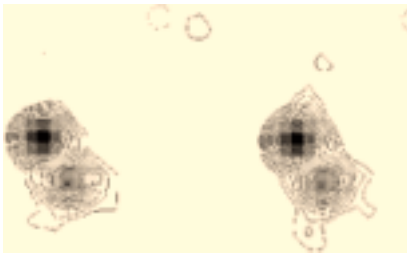

Figure 16: H-band τ CMa object reconstructions for the first (left) and second (right) 16 frames. Same contour levels as Figure 14.

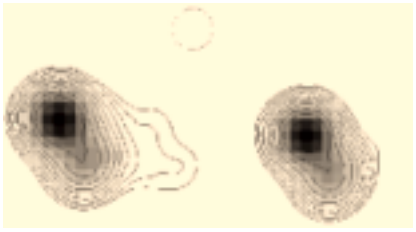

Figure 17: K-band τ CMa object reconstructions for the first (left) and second (right) 16 frames. Same contour levels as Figure 14.

el and over-sampled at the longer wavelengths easily resolving the companion. The data were taken in "speckle" mode, i.e. using a series of 200 short exposures (t_{exp} = 50 ms) with a sample time of Δt = 0.74s. Seeing was estimated to be 0.8″ at visible wavelengths (0.55μm). The AO loop was operated at maximum gain with the Shack-Hartman Reticon sensor in line mode, at a rate of 200Hz.

The initial data post-processing consisted of background correction and flat fielding with bad-pixel correction. Figure 14 shows SAA images for the three observing bands. These clearly show the companion but they are also contaminated by extended halo due to the residual wavefront errors of the AO compensation as well as a "fixed-pattern" error in the form of triangular coma giving rise to a "lumpy" Airy ring about the image cores. These clearly illustrate the need for deconvolution.

In the initial application of the algorithm, the original 200-frame data sets were reduced to sub-sets of 16 frames of 64 × 64 pixels i.e. 2.24″ × 2.24″. Thus, there were $(M+1)N^2$ = 69632 variables to be minimized for M convolution images of

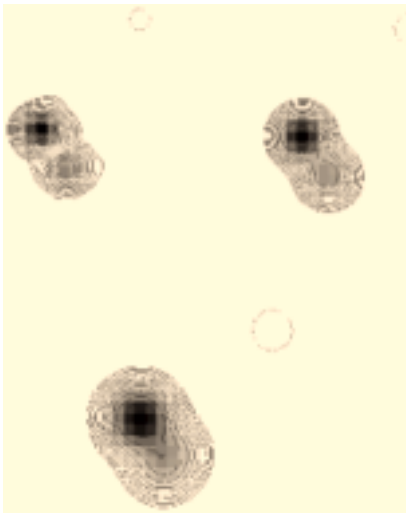

Figure 18: Final Gaussian smoothed J (top left), H (top right) and K-band (bottom) τ CMa object reconstructions using all 200 data frames and an SH start. Same contour levels as Figure 17.

size $N \times N$. For all three wavebands, the first 16 frames were used and the initial object estimates were the SAA images shown in Figure 14. As no prior PSF knowledge existed, the *initial* PSF estimates were chosen to be Gaussians. The super-resolved images were filtered back with a Gaussian of FWHM = 0.083″ which slightly over resolves the diffraction-limit at this wavelength, i.e. λ/D ≈ 0.12″. Figures 15, 16 and 17 show the reconstructed objects for the three wavebands obtained from the first and second sets of 16 frames of the 200-frame data sets. Note the strong similarity between the image pairs with differences occurring only at the few-percent level and also note how clean the reconstructions are.

Keith Hege at Steward Observatory has suggested that Speckle Holography (SH) (Hege, 1989) imposes a further constraint on the data. This is applied outside of the blind deconvolution loop and may prevent stagnation into a local minimum. It makes use of a multiple-frame data set along with PSF estimates for each frame. The object estimate was obtained as follows, i.e.

$$\hat{f}_i = \mathrm{FT}^{-1}\left[\hat{F}_u\right] = \mathrm{FT}^{-1}\left[\frac{\langle G_u \cdot \hat{H}^*_u \rangle}{\langle H_i \cdot \hat{H}^*_i \rangle}\right]$$

$$= \mathrm{FT}^{-1}\left[F_u \frac{\langle H_u \cdot \hat{H}^*_u \rangle}{\langle \hat{H}_u \cdot \hat{H}^*_u \rangle}\right] \qquad (14)$$

so that when the PSF estimates equal the true PSFs then the band-limited object estimate will equal the true band-limited object. This multiple-frame deconvolution has been shown to be less noise sensitive than deconvolving on a frame-by-frame basis. The object estimate from this procedure coupled with the PSFs, which produced it, can then be fed back into the myopic deconvolution code as new estimates.

Band	Δr (mas)	PA (°)	Δ*m*
J	149	34	0.84
H	149	33	0.80
K	149	33	0.94

Table 2: Astrometry and photometry for the 200-frame τ CMa blind deconvolutions reconstructions for the three wavebands.

For the three data sets reported here, a variant of this was performed. The PSFs for all 200 frames at each waveband were computed by simply taking the super-resolved object estimate (from the first 16-frame start-up sub-set, using Gaussian PSFs) and deconvolving into each measured data frame. These were then used as the PSF estimates in equation (2) to generate a new object estimate. Blind deconvolution was then applied to all 200 frames for each waveband. The resulting object estimates are shown in Figure 18.

These images show a very clean deconvolution with lack of background features below the 1% levels. The astrometry and photometry of the final images obtained by Gaussian fits are given in Table 2 and show very self-consistent astrometry for the three wavebands.

4.2. Io observations

The Jovian Galilean satellite, Io, is typical of the type of Solar-System objects which are benefitted by AO observations. At thermal infrared wavelengths, the volcanic hot spots can be detected against the cooler background surface without waiting for the moon to go into eclipse. Its volcanic activity is monitored from the ground using the thermal camera facility (COMIC) which is available on the ADONIS system at the ESO 3.6-m (Le Mignant et al. 1998). It was observed in September 1998 in the L' band (λ = 3.809, Δλ = 0.623 μm) with an image scale of 0.100″/pixel, corresponding to ≈ 400 km on the surface of Io, and an integration time of 500 msec. The source had a visual magnitude of m_v = 5.1, and measurements of the seeing using the Differential Image Motion

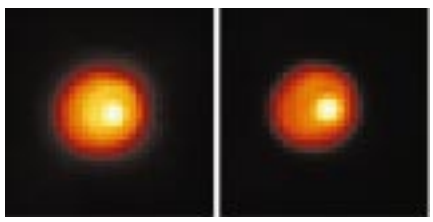

Figure 19: ADONIS imaging of Io. The ensemble average of a set of ten exposures is shown on the left and the reconstructed object is shown on the right.

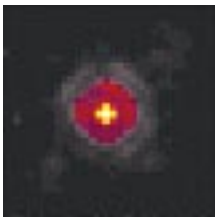

Figure 20: Ensemble average reference star (PSF calibrator) image for the Io observations.

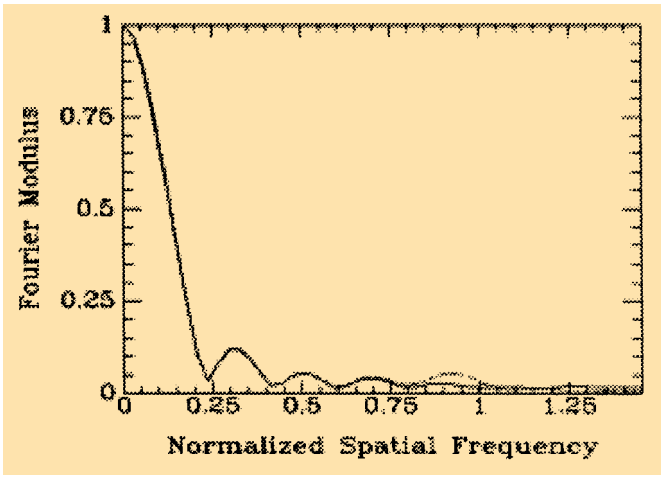

Figure 22: Azimuthally averaged radial profiles through the Fourier modulus of the pixel-limited truth image (solid-line, see Figure 24) and the reconstructed image (dashed line).

Monitor (DIMM) was 0.75″. At this wavelength the 3.6-m has a diffraction-limit of 0.226″ so that the object was well oversampled. A PSF calibrator with similar visible brightness HD174974 (m_v = 5.0, G5) was observed to yield initial PSF estimates. The field of view of the observations was 12.8″ × 12.8″.

The data set comprised ten separate observations of Io, the complete average is shown in Figure 19. This was used as the initial object estimate. The mean of the point source calibrator was used as the initial PSF estimate, shown in Figure 20. Note that the PSF is diffraction-limited with a Strehl ratio of ~ 50%.

The reconstructed object is also shown in Figure 19. This has been regularised by suppressing the high-spatial frequency information with apodisation by a perfect telescope transfer function. Thus, the effective resolution is the same as for the observation, but now the "hot spot" on the satellite's surface, Loki, is more clearly discerned against the smooth distribution of the surface.

The algorithm's ability to super-resolve has been discussed earlier. For objects with sharp edges, such as a planetary satellite or asteroid, truncation of the high spatial frequencies results in "ringing" in the image domain. The super-resolution achieved on these types of objects has been discussed previously (Christou et al., 1994) and is further illustrated below with simulations of Io imaging. Figure 21 compares a simulated Io object, i.e. a uniform disk with two hot-spots, to the reconstruction, both of them for super-resolution which is ~ 1.5 × diffraction-limited case. As can be seen, these two images (top-right and bottom-right) agree very well. Just how well, is better seen in the Fourier moduli of the truth image compared to the reconstruction before filtering. This is shown with the azimuthally averaged radial profiles in Figure 22.

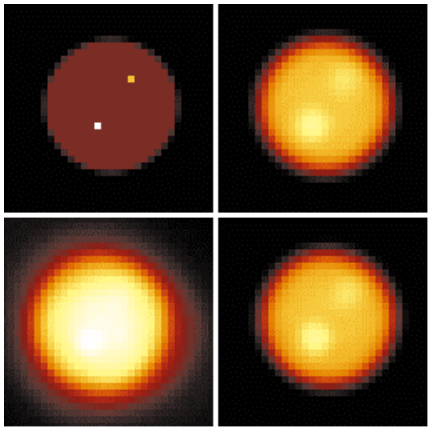

Figure 21: Simulated observations and reductions of an Io-type object: truth (top left), filtered truth (top right), observation (bottom left) and filtered reduction (bottom-right).

The radial profiles match well out to ~ 80% of the diffraction-limit where the reconstruction has greater power than the truth. Beyond the diffraction-limit, the reconstruction has non-zero power but at a lower level than the truth. The spatial frequency range shown indicates the region over which the filtered images in Figure 21 were restored.

A thorough analysis of Io adaptive optics imaging and the resulting science can be found in a recent article by Marchis et al. (1999).

4.3 R Aquarii

R Aquarii is an eclipsing symbiotic binary surrounded by morphologically complex nebulosity which extends to ~ 1 arcminute from the central source. At smaller scales, there is an elongated jet-like emission feature (Hollis et al., 1985). It was observed in December 1996 with ADONIS equipped with a Fabry-Perot at the ESO 3.6-m in both the 2μm continuum and the Hydrogen emission line, Brγ (2.1655μm) in order to detect and resolve structures of the nebulosity. The image scale was 0.05″/pixel with exposure times of 0.6s for a total integration time of 48s, for the Brγ observations reduced here. The individual frame PSNR was computed to be ~ 2000 for the central source but for the nebulosity, ~ 3″ away, it was ~ 5. In order to improve the SNR, the data were binned down from 80 to 10 frames, increasing the nebulosity SNR to ~ 15.

The 10 eight-frame-binned data were reduced using the PSF constraint (see equation 8) in addition to the band-limit and fidelity terms, where the "known" PSF was obtained from the shift-and-add image of the central source for all 80 observations. After convergence, the processing was continued with the PSF constraint removed. Figure 23 compares the nebulosity and central source for a single observation, an eight-frame average, as used for the deconvolution showing the improved SNR, and for the 80-frame sum. The reconstructed objects are shown in Figure 24 for both the Brγ and continuum observations, both with and without the PSF constraint. The initial estimate in each case was the Richardson-Lucy reconstruction. Note how after the PSF constraint is "relaxed", the morphology of the nebulosity changes to better fit the observations. This nebulosity has structure on the scale of ~ 0.1″, i.e. diffraction-limited and there are obvious structural differences between the two wavebands.

5. Discussion

In this article we have shown the effectiveness of using a multi-frame iterative myopic deconvolution technique on AO data. Using the IDAC SW on both simulations and real data, it is shown that it is a powerful tool for deconvolving AO images, to remove the effects of the uncompensated components of the PSFs

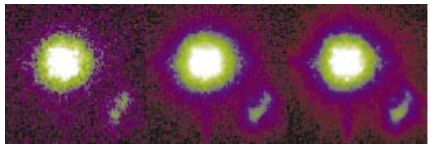

Figure 23: R Aquarii observations in Brγ. Single frame (left), 8-frame average (centre) and 80-rame average (right).

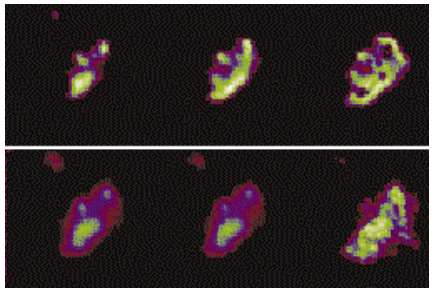

Figure 24: R Aquarii nebulosity reductions: Brγ (top) and 2 μm continuum (bottom). Left to right are the Richardson-Lucy reductions used for the initial object estimate, the PSF constrained IDAC reduction and the PSF relaxed reconstruction.

and reach full diffraction performances. The ESO ADONIS PSFs show a variability, which is common to AO systems. It is this variability and the lack of a precise frame-by-frame PSF determination that makes post-processing of the data difficult. The iterative multiframe deconvolution method described takes successfully advantage of this intrinsic variability.

The linearity of the algorithm and its preservation of photometry is demonstrated on the four star simulations.

Multi-frame iterative myopic deconvolution enforces the very important constraint that observations of the same object will yield a common object result. Some prior PSF information is extremely useful in reducing the search space for the solution as demonstrated by the R Aquarii results.

Observations of a PSF calibrator, as demonstrated here, make an excellent initial PSF estimate, and this can be further strengthened by application of the PSF constraint. A variation on this approach has been utilised by Conan et al. (1997) and Véran et al. (1997). They have demonstrated that a very good initial PSF estimate can be obtained from a statistical analysis of the residual wavefront errors. Currently, this approach is applicable only to AO systems using photon counters, but it should be extendable to wavefront sensor systems using detectors with read-out noise as well, such as CCDs. Combined statistical PSF estimation and blind deconvolution post-processing has been discussed by Fusco et al. (1998) and Christou et al. (1997).

6. Acknowledgements

We would like to thank the ESO staff at La Silla 3.6-m for the effective observing support during the observing runs. We would also like to thank Keith Hege, Matt Chesalka and Stuart Jefferies for the IDAC code and for useful discussions about its application. This work was supported by the Adaptive Optics Group of the Instrumentation Division, at the European Southern Observatory.

Bibliography

Christou, J.C., Hege, E.K., Jefferies, S.M., & Keller, Ch.U., 1994, *Proc SPIE*, ed. J.B. Breckenridge, **2200**, 433–444.

Christou, J.C., Bonaccini, D., & Ageorge, N., 1997, *Proc. SPIE*, ed. R.K. Tyson & R.Q. Fugate, **3126**, 68–80.

Christou, J.C., Marchis, F., Ageorges, N., Bonaccini, D., & Rigaut, F. 1998a, ed. D. Bonaccini & R.Q. Fugate, **3353**, 984–993.

Christou, J.C., Hege, E.K., Jefferies, S.M., & Cheselka, M., 1998b, *Proc. SPIE*, ed. A.D. Devir, A. Kohnle, U. Schreiber, & C. Werner, **3494**, 175–186.

Le Mignant, D., Marchis, F., Bonaccini, D., et al., 1998, *Proc ESO/OSA*, ed. D. Bonaccini, **56**, 287–301.

Marchis, F., Prangé, R., Christou, J.C., 1999, *Icarus*, submitted.

Fusco, T., Véran, J.-P., Conan, J.-M., & Mugnier, L.M., 1999, *Astron. Astrophys.*, **134**, 193.

Hartkopf, W.I., Mason, B.D., Barry, D.J., McAlister, H.A., Bagnuolo, W.G., & Prieto, C.M., 1993, *Astron. J.*, **106**, 352.

Hollis, J.M., Kafatos, M., Michalitsianos, A.G., & McAlister, H.A., 185, *Astrophys. J.*, **289**, 765.

Jefferies, S.M. & Christou, J.C., *Astrophys. J.*, 1993, **415**, 862.

Lucy, L., 1974, *Astrophys. J.*, **79**, 745.

Sheppard, D.G., Hunt, B.R., & Marcellin, M.W., 1998, *J. Opt. Soc. Am. A.*, **15**, 978–992.

Thiébaut, E., & Conan., J.-M., *J. Opt. Soc. Am. A.*, 1994, **12**, 485.

Véran, J.P., Rigaut, F., Maître, H., & Rouan, D., 1997, *J. Opt. Soc. Am. A.*, **14**, 3057.

LATEST NEWS

"First Light" for VLT High-Resolution Spectrograph UVES

(Excerpt from ESO Press Release 15/99, 5th October 1999)

A major new astronomical instrument for the ESO Very Large Telescope at Paranal (Chile), the UVES high-resolution spectrograph, made its first observations of astronomical objects on September 27, 1999. The astronomers are delighted with the quality of the spectra obtained at this moment of "First Light". Although much fine-tuning still has to be done, this early success promises well for new and exciting science projects with this large European research facility.

Astronomical Instruments at VLT KUEYEN

The second VLT 8.2-m Unit Telescope, KUEYEN ("The Moon" in the Mapuche language), is in the process of being tuned to perfection before it will be "handed" over to the astronomers on April 1, 2000.

The testing of the new giant telescope has been successfully completed. The latest pointing tests were very positive and, from real performance measurements covering the entire operating range of the telescope, the overall accuracy on the sky was found to be 0.85 arcsec (the RMS-value). This is an excellent result for any telescope and implies that KUEYEN (as is already the case for ANTU) will be able to acquire its future target objects securely and efficiently, thus saving precious observing time.

The three instruments foreseen at KUEYEN are UVES, FORS2 and FLAMES. They are all dedicated to the investigation of the spectroscopic properties of faint stars and galaxies in the Universe.

The UVES Instrument

The Ultraviolet Visual Echelle Spectrograph (UVES) is the first instrument on Kueyen. It was built by ESO, with the collaboration of the Trieste Observatory (Italy) for the control software. Complete tests of its optical and mechanical components, as well as of its CCD detectors and of the complex control system, were made in the laboratories of the ESO Headquarters in Garching (Germany) before it was fully dismounted and shipped to the ESO Paranal Observatory, 130 km south of Antofagasta (Chile). There, the different pieces of UVES (with a total weight of 8 tons) were carefully reassembled on the Nasmyth platform of KUEYEN and made ready for real observations.

UVES is a complex two-channel spectrograph that has been built around two giant optical (echelle diffraction) gratings, each ruled on a 84 cm $\times$ 21 cm $\times$ 12 cm block of the ceramic material Zerodur (the same that is used for the VLT 8.2-m main mirrors) and weighing more than 60 kg. These echelle gratings disperse the light from celestial objects collected by the telescope into its constituent wavelengths (colours).

UVES' resolving power (an optical term that indicates the ratio between a given wavelength and the smallest wavelength difference between two spectral lines that are clearly separated by the spectrograph) may reach 110,000, a very high value for an astronomical instrument of such a large size. This means for instance that even comparatively small changes in radial ve-

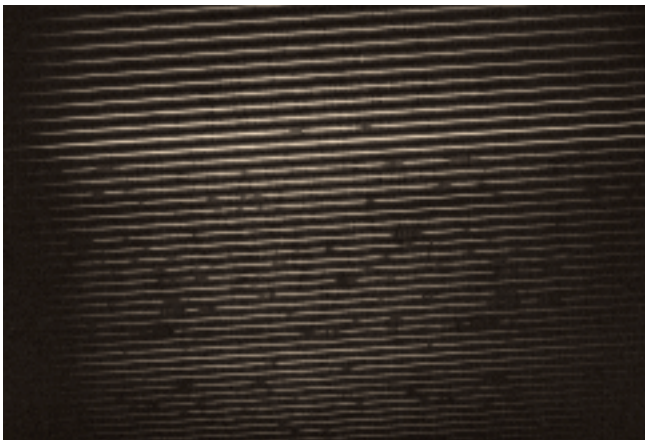

Figure 1: The power of UVES is demonstrated by this two-hour test exposure of the southern quasar QSO HE2217-2818 with U-magnitude = 16.5 and a redshift of z = 2.4. This UVES echelle spectrum is recorded in different orders (the individual horizontal lines) and altogether covers the wavelength interval between 330–450 nm (from the bottom to the top). It illustrates the excellent capability of UVES to work in the UV-band on even faint targets. Simultaneously with this observation, UVES also recorded the adjacent spectral region 465–660 nm in its other channel. The broad Lyman-alpha emission from ionised hydrogen associated with the powerful energy source of the QSO is seen in the upper half of the spectrum at wavelength 413 nm. At shorter wavelengths, the dark regions in the spectrum are Lyman-alpha absorption lines from intervening, neutral hydrogen gas located along the line-of-sight at different redshifts (the so-called Lyman-alpha forest) in the redshift interval z = 1.7–2.4. Note that since this exposure was done with the nearly Full Moon above the horizon, an underlying, faint absorption-line spectrum of reflected sunlight is also visible.

locity (a few km/sec only) can be accurately measured and also that it is possible to detect the faint spectral signatures of very rare elements in celestial objects.

One UVES channel is optimised for the ultraviolet and blue, the other for visual and red light. The spectra are digitally recorded by two highly efficient CCD detectors for subsequent analysis and astrophysical interpretation. By optimising the transmission of the various optical components in its two channels, UVES has a very high efficiency all the way from the UV (wavelength about 300 nm) to the near-infrared (1000 nm or 1 µm). This guarantees that only a minimum of the precious light that is collected by KUEYEN is lost and that detailed spectra can be obtained of even quite faint objects, down to about magnitude 20 (corresponding to nearly one million times fainter than what can be perceived with the unaided eye). The possibility of doing simultaneous observations in the two channels (with a dichroic mirror) ensures a further gain in data gathering efficiency.

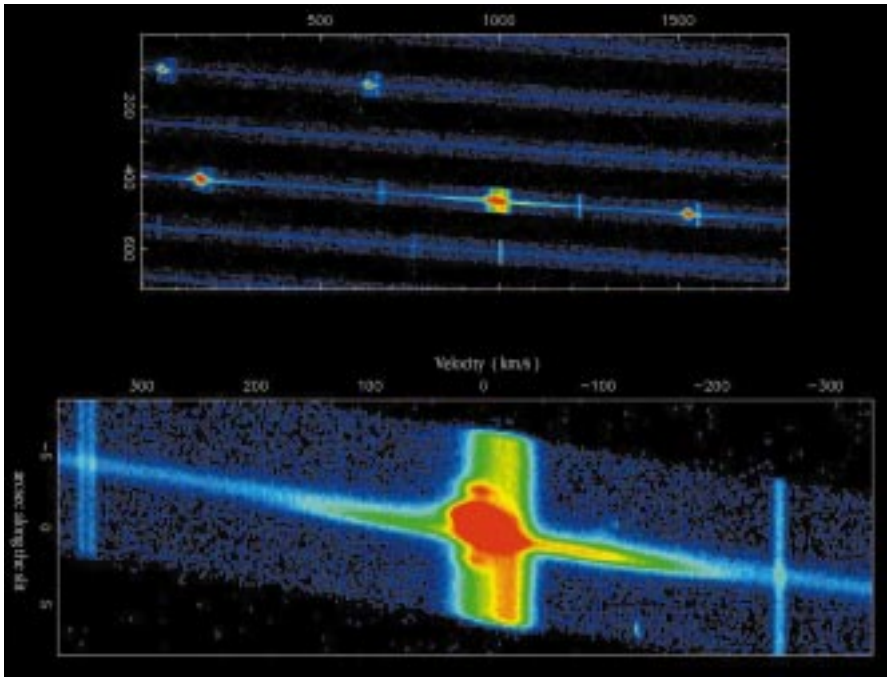

This false-colour image has been extracted from an UVES echelle spectrum of SN 1987A, with a slit width of 1 arcsec only. The upper part shows the emission lines of nitrogen, sulfur and hydrogen, as recorded in some of the spectral orders. The pixel coordinates (X,Y) in the original frame are indicated; the red colour indicates the highest intensities. Below is a more detailed view of the complex H-alpha emission line, with the corresponding velocities and the position along the spectrograph slit indicated. Several components of this line can be distinguished. The bulk of the emission (here shown in red colour) comes from the ring surrounding the supernova; the elongated shape here is due to the differential velocity exhibited by the near (to us) and far sides of the ring. The two bright spots on either side are emission from two outer rings. The extended emission in the velocity direction originates from material inside the ring upon which the fastest moving ejecta from the supernova have impacted. Finally, there is a broad emission extending all along the spectrograph slit (here mostly yellow) upon which the ring emission is superimposed. This is not associated with the supernova itself, but is H-alpha emission by diffuse gas in the Large Magellanic Cloud (LMC) in which SN 1987A is located.

First Observations with UVES

In the evening of September 27, 1999, the ESO astronomers turned the KUEYEN telescope and – for the first time – focussed the light of stars and galaxies on the entrance aperture of the UVES instrument. This is the crucial moment of "First Light" for a new astronomical facility.

Much of the time during the first observing nights was spent by functional tests of the various observation modes and by targeting "standard stars" with well-known properties in order to measure the performance of the new instrument. They showed that it is behaving very well. This marks the beginning of a period of progressive fine-tuning that will ultimately bring UVES to peak performance.

The astronomers also did a few "scientific" observations during these nights, aimed at exploring the capabilities of their new spectrograph. They were eager to do so, also because UVES is the first spectrograph of this type installed at a telescope of large diameter in the southern hemisphere.

Many exciting research possibilities are now opening with UVES. They include a study of the chemical history of many galaxies in the Local Group, e.g. by observing the most metal-poor (oldest) stars in the Milky Way Galaxy and by obtaining the first, extremely detailed spectra of their brightest stars in the Magellanic Clouds. Quasars and distant compact galaxies will also be among the most favoured targets of the first UVES observers, not least because their spectra carry crucial information about the density, physical state and chemical composition of the early Universe.

Erratum

In the June issue of *The Messenger* (No. 96), page 26 (article by H. Lamy and D. Hutsemékers), formula 2 should read:

$$q = \frac{R_q - 1}{R_q + 1} \text{ where } R_q^2 = \frac{I_0^v / I_0^i}{I_{45}^v / I_{45}^i},$$

$$u = \frac{R_u - 1}{R_u + 1} \text{ where } R_u^2 = \frac{I_{22.5}^v / I_{22.5}^i}{I_{67.5}^v / I_{67.5}^i}, \quad (2)$$

The La Silla News Page

The editors of the La Silla News Page would like to welcome readers of the fourteenth edition of a page devoted to reporting on technical updates and observational achievements at La Silla. We would like this page to inform the astronomical community of changes made to telescopes, instruments, operations, and of instrumental performances that cannot be reported conveniently elsewhere. Contributions and inquiries to this page from the community are most welcome.

News from the NTT

O. HAINAUT and the NTT Team

During the past months, many things have changed at the NTT. In June, we closed the telescope during 10 days, for a major maintenance period. During that time, our computer system was completely upgraded: the 99FEB version of the VLT software was installed, together with the latest version of the Data Flow Software. In parallel, several machines were either changed or received additional memory, making the whole system much faster. Visiting astronomers will be pleased to learn that the observer's workstation has been replaced by an HP-C360 (a very powerful machine) equipped with 50 Gb of disk for data storage and analysis. The latest versions of MIDAS, IRAF, IDL and eclipse are installed and running on this machine. A consequence of the workstation upgrade is that P2PP (the "Phase II Preparation Programme" used to prepare the observations) is running much faster: one no longer has to wait several seconds for a pop-up to appear. The La Silla software team did a great job at installing this software with the help of colleagues from Garching and Paranal. At this time, there are still a few details to be ironed out (e.g. a problem of compatibility between the new software and the old time distribution cards on the axes computers), but they should be solved soon, and have no major impact on the operation.

During the June technical time, all the telescope optics were maintained: Alain Gilliotte washed the main and tertiary mirrors with soap and water (cf. Fig. 1). The result is excellent: M1's reflectivity is back to 89.5%, while it was 90.1% right after its last aluminisation two years ago. The micro-roughness of the mirrors was not fully restored by the washing: it is now 37Å, instead of 10Å after aluminisation. We are investigating the consequences of this change on the diffused light. The secondary mirror was also aluminised.

EMMI and SUSI2 received a complete optomechanics maintenance: all the optics were cleaned, and some motors were changed. The dichroic used in EMMI-DIMD was inspected, as it was suspected to cause some problems, but was found in good shape. SUSI's M4 (the pick-up mirror) was found to have a damaged coating; the whole mirror is being replaced. Various narrow band filters just arrived for SUSI2: Hα, Hα (6000 km/s), Hβ, Hβ (6000 km/s), O III and He II. They will be tested and hopefully offered soon to the observers.

SOFI has been misbehaving over the past months: the liquid Helium closed-cycle cooler failed just before the technical time (during which it was supposed to be maintained!), causing the complete loss of three nights. After its replacement, it was discovered that part of the instrument was not properly cooled. This new problem is being investigated, and will force us to re-open the instrument soon. In the meantime observations are not disrupted as we use the LN2-based pre-cooling system.

A new GPS board arrived to replace the one we are currently using for our time reference. In August the week counter of the general GPS system will reach the critical value of 1023, then restart at 0. Our GPS, as most of those more than a few years old, cannot deal with this change and will find itself back in the late 1970s. After changing a chip in our old board, we will keep it as a spare.

From the operational point of view, the past months have seen the implementation of a detailed plan of preventive maintenance. Every day, a scheduler provides us with a list of items to be verified and, in most cases, we just have to run a "template" which performs a series of measurements, and generates a plot and diagnostics.

The NTT is still operated with a team that is short of one astronomer, who should replace Chris Lidman (who left for the VLT) as SOFI instrument scientist. During the first six months of the year, the fellows were asked to perform extra duty days at the telescope to ensure full support of each SOFI run, but in August, we will have to offer this instrument with minimum support. We hope to recruit an additional astronomer in the coming months.

Ismo Kastinen recently joined the team as our 6th Telescope and Instrument Operator. This will allow us to run the telescope most of the time with a day, a night, and a day/night operator. This configuration provides the necessary manpower to perform the operations required by the calibration and maintenance plans.

During the coming months, we plan to update the EMMI and SUSI observation templates. As these were written at the time of the "Big Bang" (the 1996–1997 one, not the cosmological one), and as they were the first observation templates ever written, they are far from ideal from an operation and maintenance point of view. We hope to be able to offer the new ones early next millennium.

Figure 1: Alain Gilliotte, optician engineer at La Silla, is starting to wash the NTT main mirror, with a solution of soap and water and a sponge.

3.6-m Telescope Control System Upgrade Completed

M. STERZIK, U. WEILENMANN, and the 3.6-m Upgrade Team

New highlights can be reported from the 3.6-m upgrade project: the full VLT-compliant Telescope Control System (TCS) has been finally tested and commissioned during recent technical-time periods. On August 9th it has been successfully put into routine operation. Let us briefly recall the milestones passed. The "heart" of the telescope, the servo control system for the axis, was completely modified. The telescope control is now based on so-called “Local Control Units” (LCUs), an identical hardware platform to that used at the VLT. It substitutes the over 20 years old TCS running on HP1000 computers. In contrast to the VLT and NTT, the 3.6-m is an equatorial mounted telescope, and the entire control SW had to be modified and adapted for controlling the alpha and delta axis. With the broad usage of standardised architectures and software concepts at the 3.6-m, which were originally designed and developed for the VLT, we intend to gain operational stability, quality, and maintainability. However, it also requires to replace proven components like the old, incremental encoders with optical strip encoders which are required to read the telescope position. The new encoders are supposed to deliver a five times higher resolution, but once we tested the performance of them in practice, we encountered an unexpected problem: in extreme telescope positions, implying several tens of tons of weight on the axis, the tight tolerances (±100 mm) required for reliable readings of the position were exceeded, thus loosing control over the telescope. Through careful adjustment of the heads we were able to restrict the “dead zone” to a very small region in the Northwest. In September, a dynamical mount for the reading heads will be installed, which is expected to completely solve this problem.

Work is also proceeding on other system components: The manual telescope control and the interlock system is being upgraded and adapted to the new control environment. The Infrared configuration (f/35) is being prepared for the arrival of TIMMI2 early next year and the CES refurbishment and upgrade is due in October. There are still minor issues to be clarified in order to fully understand the behaviour of the telescope. To maintain the already excellent image quality of less than 0.6 arcsec, both, operational and maintenance procedures have to be implemented and also an improvement of the f/8 top-end is presently being studied. All in all, close to 40 FTEs will have been invested into the upgrade of the 3.6-m telescope, and La Silla has gained vast experience in operating and maintaining VLT-era telescopes.

What do all these upgrades mean to the user, the visiting astronomer? First of all, the pointing and tracking performance is dramatically improved: a remarkable pointing accuracy of 5 arcsec rms is now achieved, and the drift rate is well below 1 arcsec per 10 minutes during free tracking, a value that was out of reach for the old system. In combination with the new TCS, the entire VLT-compliant software presently running in the 3.6-m was upgraded to the VLT-FEB99 Common Control Software release, implying full Y2K compliance of the system. With the help of DMD the archiving part of the data flow system (DFS) was implemented. All frames obtained with the EFOSC2 instrument are transferred via standard VLT/DMD data handling tools to a centralised La Silla archive, where compact disks are produced for each observing night. The use of the DFS also allows us to implement a data reduction pipeline, which we plan to offer for the most commonly used modes of EFOSC2 in the near future. It also allows us to enhance our instrument calibration database, and to ease data quality control checks.

Maybe the most important improvement in the 3.6-m that comes with the upgrade is its gain in operational stability and in the reduction of technical downtime. Beside the more reliable electronics used, the strict implementation of formalised procedures and checklists for daily start-ups, instrument set-ups and change-overs lead to a constant and significant decrease in downtime, comparing the 7% in 1998 (corresponds to 140 hours of total available observing time lost due to technical problems) with the 4% in 1999 (January–July, 60 h). In view of these numbers we ask the visiting astronomer to forgive us the inconvenience of finding the 3.6-m telescope building locked (like the NTT), which requires to call the operator on duty to grant access to the building. But also this action helps us to keep configuration control.

Finally we are happy to announce a new, very detailed EFOSC2 manual, including a description of the “neo-classical” observing strategy. It is available from the 3.6 Web pages (http://www.ls.eso.org.lasilla/Telescopes/360cat/efosc/html/doc/EFOSC2manula.ps.gz), and we invite all EFOSC2 observers to consult this manual in advance of their observations.

Without the constant enthusiasm and personal commitment of all the people involved, in particular the technical support teams at La Silla, the 3.6-m upgrade project would never have reached the current level of quality and success.

3.6-m Telescope Blind Tracking Performance

First Detection of the Methane Field Brown Dwarf SDSS 162414.37+002915.6 in i-Band

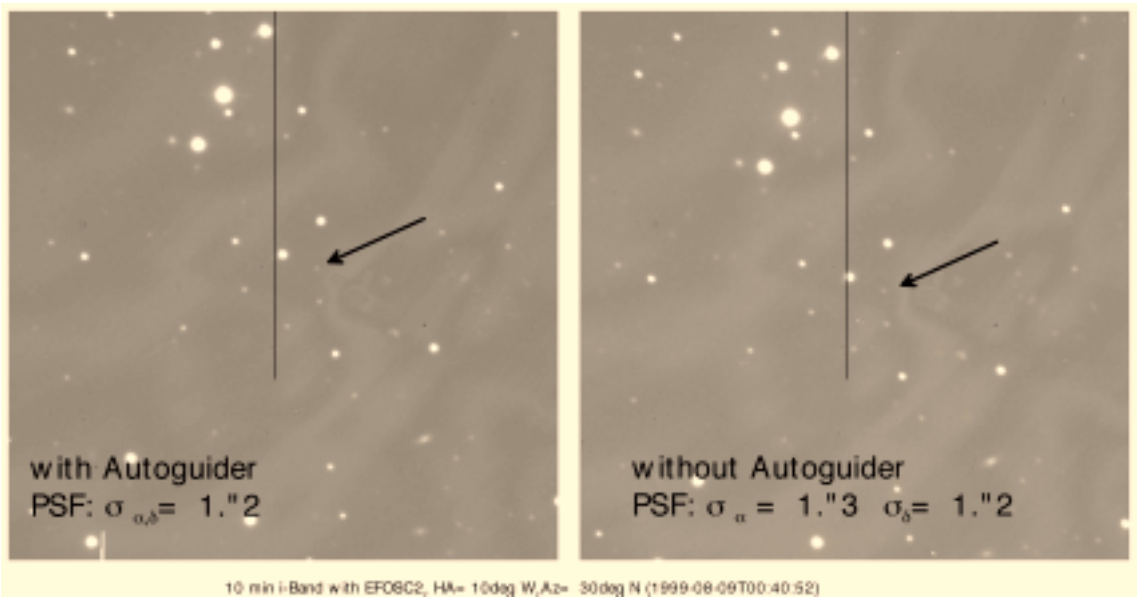

Deconvolving Spectra of Lensing Galaxies, QSO Hosts, and More . . .

F. COURBIN[1,2], P. MAGAIN[2], S. SOHY[2], C. LIDMAN[3], G. MEYLAN[4]*

[1]Universidad Católica de Chile, Departamento de Astronomía y Astrofísica, Santiago, Chile
[2]Institut d'Astrophysique et de Géophysique, Liège, Belgium
[3]European Southern Observatory, Chile
[4]European Southern Observatory, Garching
**Also Maître de recherches au FNRS (Belgium)*

1. Background and Motivation

High spatial resolution undoubtedly plays a key role in most major advances in observational astrophysics. In this context, considerable effort has been devoted to the development of numerical methods aimed at improving the spatial resolution of astronomical images. However, the most commonly used techniques (e.g., Richardson 1972, Lucy 1974, Skilling & Bryan 1984) tend to produce the so-called "deconvolution artefacts" (oscillations in the vicinity of high spatial frequency structures) which alter the photometric and astrometric properties of the original data. Recently, Magain, Courbin & Sohy (1998ab; hereafter MCS) proposed and implemented a new deconvolution algorithm which overcomes such drawbacks. Its success is mainly the consequence of a deliberate choice to achieve an improved resolution rather than an infinite one, hence avoiding retrieving spatial frequencies forbidden by the sampling theorem.

Many successful applications of the MCS algorithm have been carried out in the framework of an intensive effort to obtain detailed light/mass maps for lensing galaxies (e.g., Courbin et al. 1997, 1998ab, Burud et al. 1998abc). These results, when compared with recent Hubble Space Telescope (HST) images, clearly demonstrate the effectiveness of the method in producing reliable high-resolution images.

High angular resolution is certainly a must in imaging, but it is also of great interest in spectroscopy. From realistic simulations, we illustrate here a promising spectroscopic version of the MCS algorithm. We demonstrate that flux-calibrated spectra of severely blended objects can be accurately extracted and show how the algorithm can be used to decontaminate the spectra of extended objects from the light of very nearby bright point sources. The preliminary deconvolution of near-IR NTT (SOFI) spectra of the lensed QSO HE 1104-1805 are presented as an example of an application to real data. The faint spectrum of the lensing galaxy is clearly unveiled by the deconvolution algorithm.

2. Spatial Deconvolution of Spectra

MCS have shown that sampled images should not be deconvolved with the observed Point Spread Function (PSF), but with a narrower function, chosen so that the final deconvolved image can be properly sampled, whatever sampling step is adopted to represent it. For this purpose, one chooses the final (well-sampled) PSF of the deconvolved image and computes the PSF which should be used to perform the deconvolution and which replaces the observed total PSF.

Depending on the resolution which is aimed at, the width of such a profile may be anything between "slightly narrower" than the observed PSF or seeing (this results in a very high but not infinite gain in resolution), and critically sampled width, which would result in a modest gain in resolution. A straightforward consequence of choosing the shape that the PSF will have in the deconvolved image is that it is, indeed, exactly known. Such prior knowledge can be used to decompose the data (image or spectrum) into a sum of point

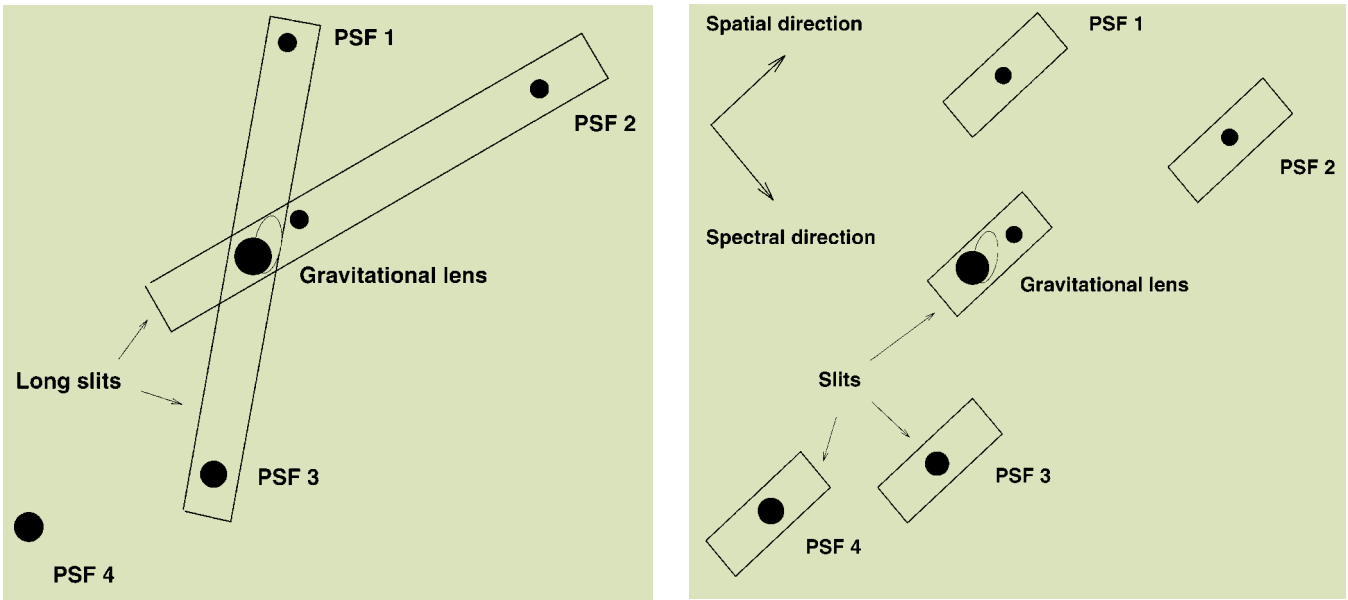

Figure 1: Two possible instrumental set-ups to obtain simultaneously the spectra of the object of scientific interest (a lensed QSO in the present example) and that of one or more PSF stars. Left: long slit spectroscopy. Right: Multi Object Spectroscopy. The latter allows one to observe several PSF stars, whatever Position Angle is selected to observe the target.

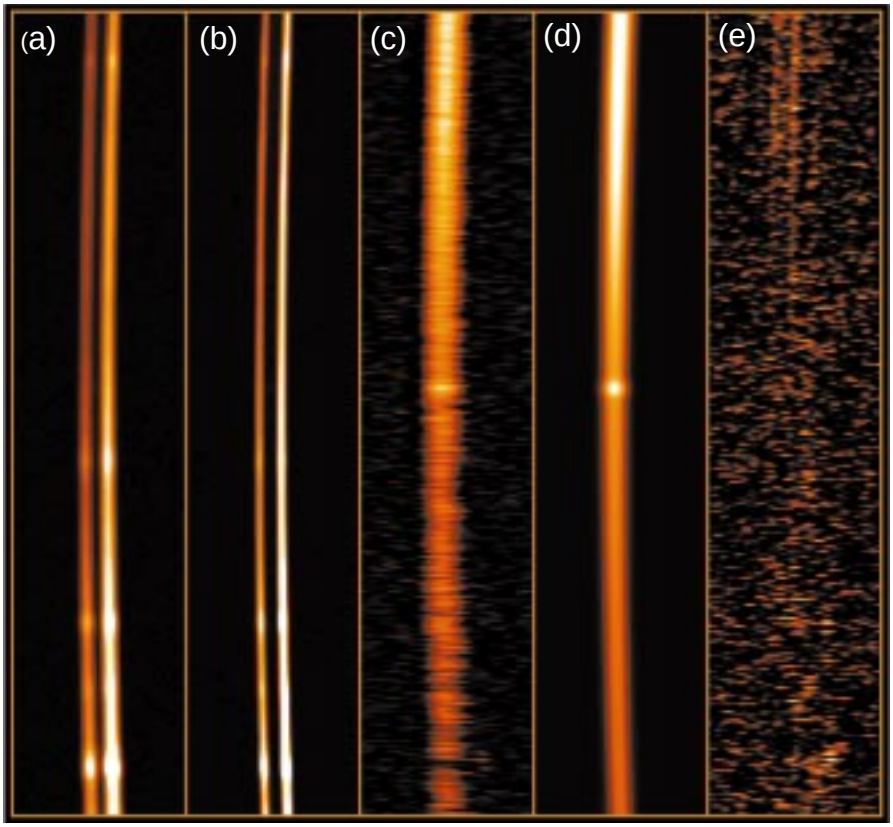

Figure 2: From left to right: (a) Simulated spectrum of a lensed quasar (~ 4000–8000 Å), (b) its deconvolution, (c) the deconvolved background (here, the lensing galaxy alone), (d) the galaxy used to construct the simulation, and (e) the residual image (data minus model) in units of the photon noise. The simulation considers seeing variation with wavelength and (exaggerated) atmospheric refraction.

sources with known analytical spatial profile, and deconvolved numerical background. This decomposition was successfully used in the MCS image deconvolution algorithm. We applied the same fundamental rule to construct an algorithm for the spatial deconvolution of spectra, as described in detail in Courbin, Magain, Kirkove & Sohy (1999).

As with the image deconvolution algorithm, precise knowledge of the instrumental profile is required. This profile varies with wavelength and time. It may be obtained in practice by aligning simultaneously on the slit, both the object of scientific interest and one or several point sources. Whenever the target is multiple (this is indeed likely if deconvolution is required), no reference point source may be observable on the same slit, as the position angle of the spectrograph is in such a case imposed by the geometry of the target. This is no more true when observing in MOS mode, where several PSF stars can be observed at the same time and used to improve the spatial sampling of the spectra, to reach even higher spatial resolution and to achieve more accurate point/extended sources decomposition. Then, finding suitable PSF stars is not more a limitation in spectroscopy than in imaging. Figure 1 shows two examples of instrumental set-ups which may be adopted to yield observations well suited to the problem of spectra deconvolution.

In order to minimise the effect of the PSF variation across the field, PSF stars should be selected as close to the main target as possible. Observing several such point sources will not only allow oversampling of the deconvolved spectra, but also to check whether a given reference star is multiple or not, and to check the PSF stability over the field. Even if the algorithm can cope with critically sampled data, detectors with small pixel sizes should be preferred (e.g., the high-resolution collimator of FORS1/FORS2 provides 0.1″ pixel, which is exceptionally small for a spectrograph), and high signal-to-noise ratio aimed at. The above conditions are in fact the same as in imaging. Good sampling, PSF stability and high signal-to-noise are definitely the main requirements when performing photometrically (spectrophotometrically in the present case) accurate deconvolutions.

In practise, the deconvolved PSF (i.e., shape of the point sources in the deconvolved spectra) can be as narrow as one may wish, the only theoretical limitation to the gain in resolution being the sampling of the deconvolved data. In our implementation of the algorithm, one can improve the pixel size (in the spatial direction) by a factor 2, so that the maximum resolution will be 2 (half) CCD pixels FWHM. This limit can in principle be reached, whatever seeing is available in the data spectra, although, as one can expect, the quality of the result decreases as the seeing increases.

3. Simulations

The algorithm has two obvious applications: firstly, to extract the individual spectra of strongly blended point sources and, secondly, to unveil the spectra of extended objects hidden by much brighter point sources. While de-blending point sources is relatively easy (see Courbin, Magain, Kirkove & Sohy 1999 for an example), the most interesting applications of our spectrum deconvolution algorithm may consist in its capability to decompose spectra into the components from point sources and extended sources. The two simulated spectra presented hereafter illustrate the results that can be expected from high signal-to-noise data.

Our simulations include slit misalignment, seeing variation as a function of wavelength as well as – exaggerated – atmospheric refraction. Gaussian photon noise and readout noise are also added to the data. A typical signal-to-noise ratio is 200–300 per spectral-resolution element. The PSF is derived from the simulated spectrum of a point source whose S/N ratio is similar to the one of the scientific data. The deconvolutions are performed as in imaging and the optimal choice of the different Lagrange multipliers to be used is guided by the visual inspection of the residual maps (RM) (see Burud et al. 1998b for an example of a RM). The RM is the absolute value of the difference between the raw data and the deconvolved image reconvolved by the (narrower) PSF, in units of the noise. An accurate deconvolution should therefore correspond to a flat RM with a mean value of 1.

3.1 Simulated lens and QSO host galaxies

Figure 2 presents the simulated spectra of two lensed images of the same quasar, separated by 6 pixels in the spatial direction. The spatial resolution is 4 pixels FWHM and the signal-to-noise ratio of the brightest spectrum is about 200–300 per spectral resolution element, depending on the wavelength. The flux ratio between the two QSO images is 3 (1.2 magnitudes). The spectrum of the – extended – lensing galaxy is also incorporated in the simulated data. It is located only 2 pixels away from the centroid of the faintest QSO image and is about 3 to 5 magnitudes fainter than the QSO images (depending on wavelength) and therefore completely invisible in the raw data (see left panel of Figure 2). The second panel shows the result of the deconvolution, the third panel displays the 2-D deconvolved spectrum of the lensing galaxy alone, which compares very well with the original simulated spectrum shown in the fourth panel. The RM, as defined at the beginning of this section, is displayed

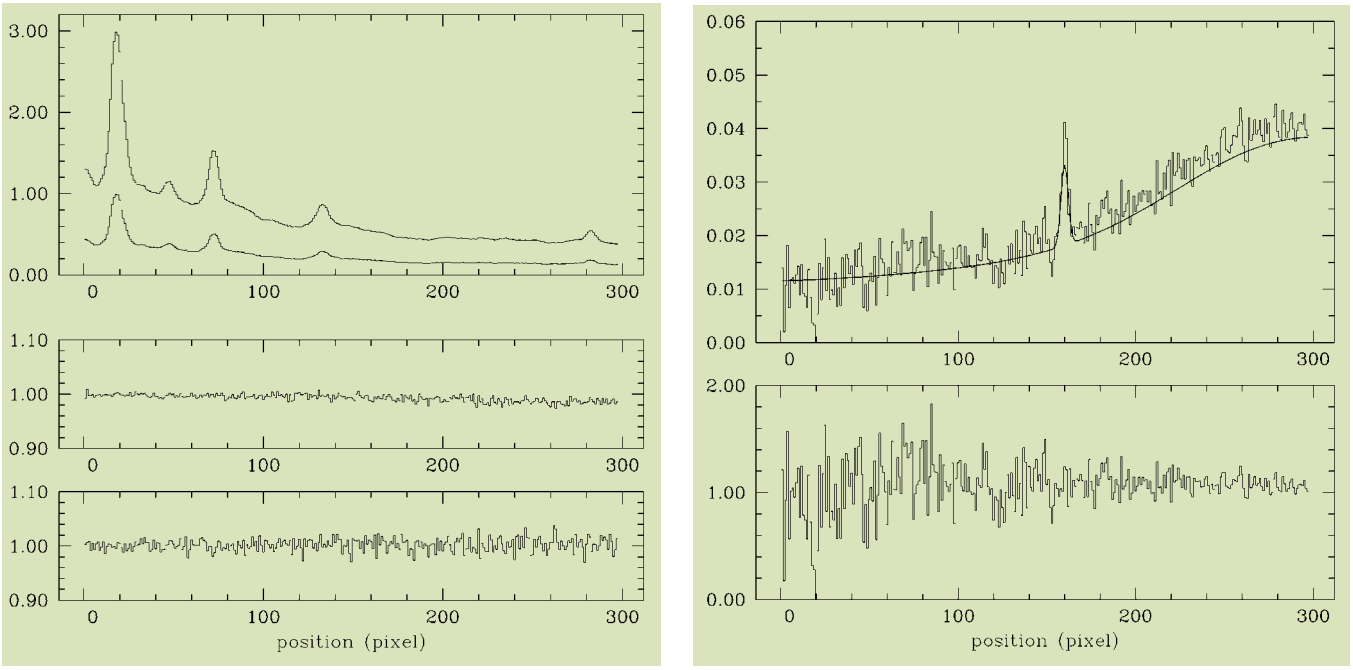

Figure 3: ***Left:*** *The top panel shows the 1-D deconvolved spectra of the two simulated QSO images. In the middle and bottom panels are displayed the flux ratios between the two spectra and the original QSO spectrum used in the simulation.* ***Right:*** *the spectrum of the lensing galaxy alone (top) and its division by the input spectrum (bottom). The position of the emission line is retrieved with an accuracy of 0.1 pixel.*

in the last panel and does not show any significant structure, as expected for a good deconvolution.

Figure 3 confirms the good results obtained in Figure 2. The 1-D spectra of the 2 QSO images as well as the spectrum of the lensing galaxy are in very good agreement with the input spectra (solid line), in spite of the blending and high luminosity contrast. The emission line in the spectrum of the lensing galaxy is well recovered and its (spectral) position is retrieved with an accuracy of 0.1 pixel.

A more difficult application may consist of the spectroscopic study of QSO host galaxies. In this case, a bright QSO is centred almost exactly on the bulge of a much fainter host galaxy, which can sometimes be imaged with standard techniques. We have tested the spectroscopic version of the MCS algorithm on such a difficult case, and show from the results in Figure 3 that the spectrum of a host galaxy can be accurately decontaminated from light pollution by its central AGN. The host galaxy in our example is about 2 magnitudes fainter than the QSO and has the spatial extension of a low redshift galaxy (z = 0.1–0.3).

3.2 A near-IR spectrum of the lensing galaxy in HE 1104–1805

We recently obtained with SOFI, mounted on the NTT, near-IR spectra of the so-called “double Hamburger”, i.e., the doubly imaged gravitationally lensed QSO HE 1104–1805 (Wisotzki et al. 1993), discovered in the Hamburg survey for bright

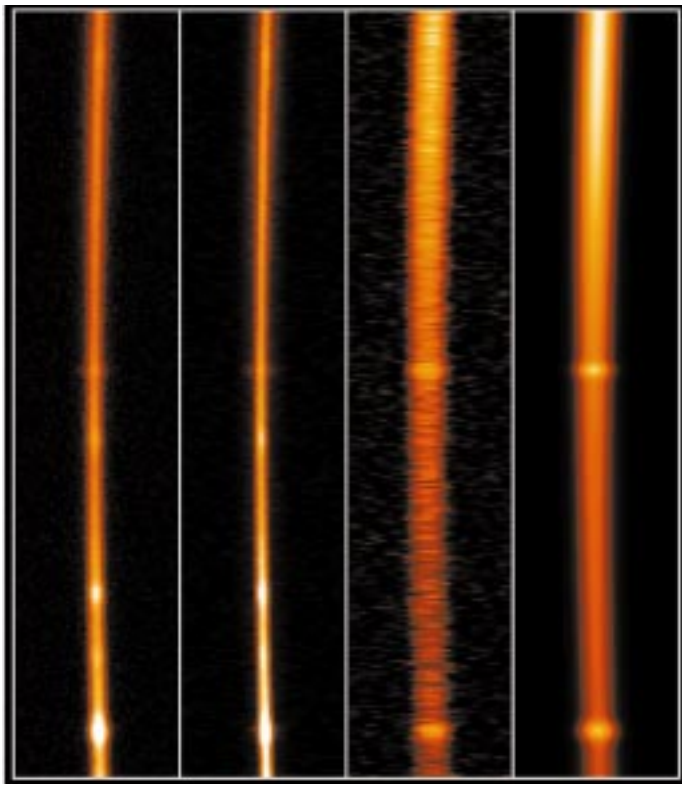

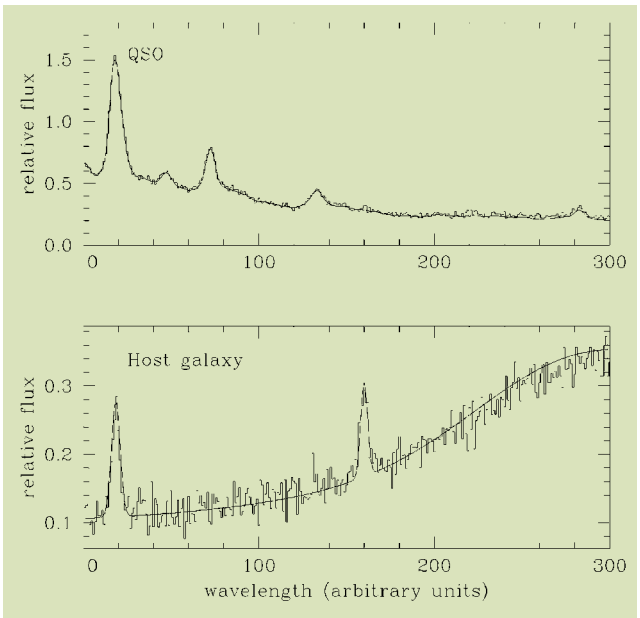

Figure 4: ***Left:*** *The two left panels display a 2-D simulated spectrum of a QSO and its host galaxy. The two right panels compare the 2-D deconvolved spectrum of the host galaxy alone, with the spectrum used in the simulation.* ***Right:*** *1-D deconvolved spectra of the QSO (top) and of the host galaxy (bottom). In each case, the solid line indicates the 1-D original spectrum used to make the simulated data.*

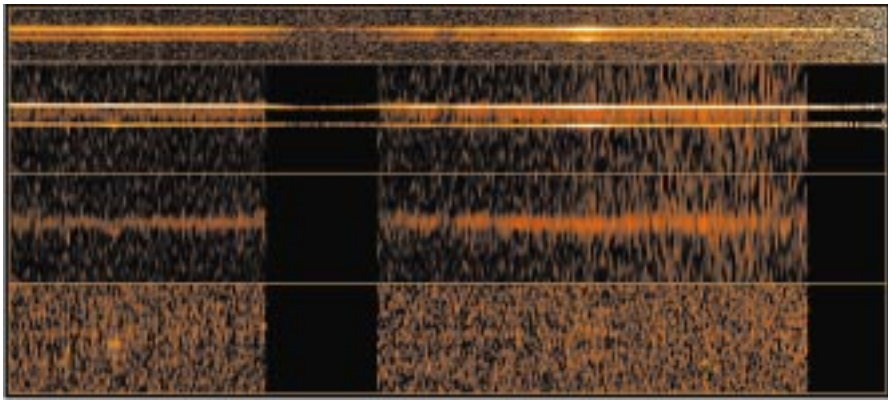

Figure 5: From top to bottom: A near-IR spectrum of the lensed QSO HE 1104–1805, between 1.5 µm (left) and 2.5 µm (right). The seeing is 0.6–0.7 arcsec and the lensing galaxy is situated about 0.5″ away from the brightest QSO image. The spectrum is deconvolved down to a resolution of 0.3″ with improvement of the sampling in the spatial direction. The third panel displays the spectrum of the lens alone and the last panel shows the residual map (RM, see text) in unit of the photon noise, to illustrate the good agreement between the data and their deconvolution. The dark areas are not used, because of strong atmospheric absorption.

QSOs and for which the time delay has been reported (Wisotzki et al. 1998). However, the redshift of the main lensing galaxy remains unknown, which still hampers any attempt to estimate H_0 from this system. As the lensing galaxy is very red (e.g., Courbin et al. 1998b), near-IR spectroscopy appeared an obvious way of determining its redshift.

SOFI spectra were obtained at the NTT between 0.9 and 2.5 microns under good seeing conditions (about 0.6–0.7″) and deconvolved down to a resolution of 0.3″. As no PSF star was observed, the PSF was computed directly from the spectra of the two QSO images (more details about this procedure are given in Courbin et al. 1999). Figure 4 shows the results of the deconvolution performed between 1.5 and 2.5 microns, since the lens is too faint in the 0.9–1.5 micron region. The original data are shown in the top panel of Figure 4. The three other panels, from top to bottom, show the deconvolved spectra with improved sampling (0.145″/pixel) in the spatial direction (this is why the width of the deconvolved 2-D images is twice that of the raw data), the spectrum of the lensing galaxy, as well as the RM (flat with a mean value of 1). The data presented here have a much lower S/N than in the simulations but are sufficient to unveil the spectrum of the faint lens. Since no emission line is detected, we are still left without precise measurement of the lens redshift. However, the prospect of measuring this redshift with optical/near-IR spectroscopy is good: with the improved S/N, sampling, and spectral resolution of future VLT data!

4. Future Prospects

Our new extension to spectroscopy of the MCS image deconvolution algorithm obviously has a wide field of applications. The most original and promising ones may consist in spectroscopic studies involving extended objects hidden by – often brighter – point sources. We have presented an application of the method to gravitationally lensed quasars, where the spectrum of a very faint lensing galaxy can be extracted. A similarly interesting application will be to take full advantage of the ability of the algorithm to decompose spectra, in order to carry out the first systematic spectroscopic study of quasar host galaxies. With current instrumentation mounted on 8–10-m-class telescopes, sufficiently high signal-to-noise spectra can be obtained, at least for low-redshift quasars, in order to derive precise rotation curves of their host galaxy, provided the spectrum of the bright QSO nucleus can be removed accurately. The present spectrum deconvolution algorithm is very well suited for such a purpose and may therefore allow significant progress, not only towards the measurement of the mass of the central black hole in QSO host galaxies, but also in astrophysics in general. We intend to release in the near future a documented public version of our image deconvolution algorithms, followed latter by the spectroscopic version of code illustrated in the present article.

Acknowledgements

F. Courbin acknowledges financial support through the Chilean grant FONDECYT/3990024. S. Sohy is supported by contracts ARC 94/99–178 “Action de Recherche Concertée de la Communauté Française (Belgium)” and “Pôle d’Attraction Interuniversitaire” P4/05 (SSTC Belgium).

References

Burud, I., Courbin, F., Lidman, C., et al. 1998a, *ApJ*, **501**, L5.

Burud, I., Courbin, F., Lidman, C., et al. 1998b, *The Messenger* **92**, 29.

Burud, I., Stabell, R., Magain, P., et al. 1998c, *A&A*, **339**, 701.

Courbin, F., Magain, P., Keeton, C.R., et al. 1997, *A&A*, **324**, L1.

Courbin, F., Lidman, C., Frye, B., et al. 1998a, *ApJ*, **499**, L119.

Courbin, F., Lidman, C., Magain, P., 1998b, *A&A* **330**, 57.

Courbin, F., Magain, P., Kirkove, M., Sohy, S., 1999, *ApJ*, in press.

Courbin, F., Lidman, C., Meylan, G., Magain, P., 1999, in preparation.

Lucy, L. 1974, *AJ*, **79**, 745.

Magain, P., Courbin, F., & Sohy, S. 1998a, *ApJ*, **494**, 472.

Magain, P., Courbin, F., & Sohy, S. 1998b, *The Messenger* **88**, 28.

Richardson, W.H.J. 1972, *J. Opt. Soc. Am.*, **62**, 55.

Skilling, J., & Bryan, R.K. 1984, *MNRAS*, **211**, 111.

Wisotzki, L., Koehler, T., Kayser, R., Reimers, D., 1993, *A&A* **278**, L15.

Wisotzki, L., Wucknitz, O., Lopez, S., Sorensen, A, 1998, *A&A* **339**, L73.

Emission-Line-Object Survey in the LMC with the WFI: New Faint Planetary Nebulae

P. LEISY[1], P. FRANCOIS[1,2], and P. FOUQUÉ[1,3]

[1]European Southern Observatory, Santiago, Chile; [2]Observatoire Meudon DASGAL, Paris, France
[3]Observatoire Meudon DESPA, Paris, France

1. Introduction

Until now, all emission-line-object surveys in the two Magellanic Clouds (MCs) have been made with Schmidt plates, either with prism objective or with the 2-filter (ON, OFF) method. The only deep survey, dedicated to the central part of the MCs, dates from 1980, and suffers from large biases because it was done using only two filters to select the candidates (about 30% of false candidates). No

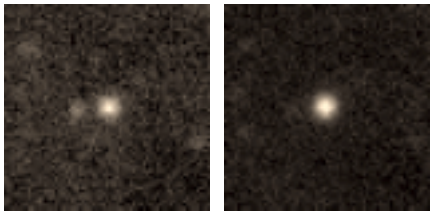

Figure 1: PN1 in Hα and [O III]. Note the high excitation object (ratio [O III]/Hα = 10).

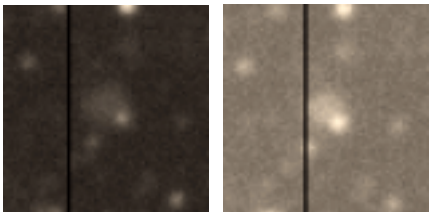

Figure 2: PN 2 in Hα and [O III]: extended object ~ 2.5″ (or 0.6 pc).

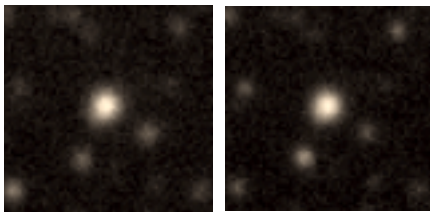

Figure 3: PN 3 in Hα and [OIII] Low excitation object.

large emission-line survey has been published with CCD devices until now.

Our final goal is a large survey (10 square degrees in total) of two regions in the SMC and the LMC, to identify new fainter emission-line objects (as PNe, HII regions, Be stars, symbiotic stars, young stars, etc.).

We concentrate our efforts mostly on PNe and HII regions. The new candidates will allow us to derive accurately the full PNe luminosity function in the Magellanic Clouds (MCs), which is still poorly known for faint objects.

Imaging with the WFI will hopefully be followed up with EFOSC2 and/or FORS to take, for the first time, spectra of the new very faint PNe but also the close-by HII regions, in order to determine the physical properties and accurate abundances of these emission-line objects.

2. Overview

LMC and SMC are ideal targets for at least three reasons:

– they are close enough so that we can have a good spatial resolution and very good S/N spectra

– their PNe and HII regions are bright enough so that a detailed analysis of their chemical composition is feasible with the current instrumentations.

– the metallicities are lower than our Galaxy

The study of all types of PNe (with different brightness, age and metallicity) is one of the cornerstone of our understanding of Intermediate-Mass Stars and the chemical evolution of galaxies. PNe are used as probes to determine the past abundances of the progenitor stars and also the current abundances of the light elements released at the end of the AGB.

The faintest PNe are also of interest because they contain two important classes of objects. Either they are old objects (low mass with longer lifetime) which gives information on the chemical composition at the early stages of the galaxy (to trace the chemical evolution over the past 10 billion years) or they are objects at the very end of their evolution in a state which allows us to look into deeper layers of their envelope.

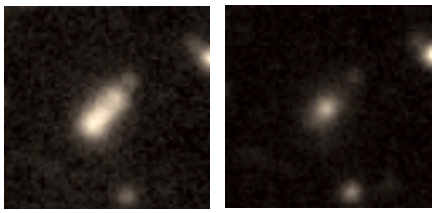

Figure 4: PN 4 in Hα and [O III]: Bipolar extended object ~ 5″ in Hα, but more compact in [O III].

To improve our understanding of the chemical evolution of the nearby galaxies, it is crucial to use the largest spatial, temporal and metallicity coverages. The PNe will help us in our understanding of the enrichment processes in He, C, N in the Intermediate-Mass stars, because they tell us about the dredge-up mechanisms occurring during the last stages of evolution of intermediate-mass stars and how they depend on the metallicity. Helium, Nitrogen, and Carbon are, directly manufactured by the PNe's star and their abundances thus provide the yield of those elements in the corresponding galaxy. In particular, we have shown in the Magellanic Clouds (Leisy and Dennefeld,1996), in a sample of 70 objects, that enrichment or destruction are strongly metallicity dependent. We obtain metallicity relations, but they are still hampered by the too few studied objects, particularly in the very low metallicity range. The Nitrogen and Carbon production are by far more effective when the initial metallicity is low. Apparently, in the SMC, the lower-mass stars produce also Oxygen, but our results are based on a small sample (8 objects).

These abundances have also been directly compared with those of adjacent HII regions which provide “recent” abundances. Until now, only very old, inhomogeneous, data are available in some galaxies, and moreover, the number of studied HII regions is always too small for a detailed comparative study. They come from various authors, are of poor quality (the forbidden emission line [OIII] λ4363Å is often missing or its uncertainty is greater than 50%). Moreover, in a given galaxy, the metallicity determined from HII regions shows a large dispersion. The metallicity determinations have mostly been based on the abundances of Oxygen because it is easily measured by optical spectroscopy. However, it may not be representative of the metallicity of the object since the ejection of various elements from stellar wind, Supernovae and Planetary Nebulae involves different times and length scales. The existence of spatial inhomogeneities in the distribution of various chemical elements within a HII region is still a matter of debate.

As the information coming from PNe and HI regions is by far uncomplete and biased to the brightest objects, a survey of PNe's and HII regions in nearby galaxies is necessary to derive proper chemical abundances and check the different elements as metallicity indicators.

3. Observations

The main advantage of using WFI over existing “uncomplete surveys” is that it provides a high spatial resolution (pixel size 0.24″) which is mandatory in such crowed regions. Moreover a large deep survey of emission-line objects in the MCs can be done covering several degrees. Our data provide at the same time: accurate positions (~0.2″) catalogue and finding charts, and the absolute fluxes. Nevertheless, this observation step is needed to prepare further observations with bigger or space telescopes, which require accurate positions and photometry in order to save as much observing time as possible.

Three nights were allocated at the beginning of January 1999, but because the 2.2-m WFI was offered in February with delay to the community, we got two nights in March and could only observe the LMC.

The two nights (March 3rd and 4th, 1999) were photometric with an average seeing of about 1.0″ (from 0.8″ to 1.3″) at airmasses between 1.3 to 1.9.

We observed three spectrophotometric standard stars per night in order to calibrate the images in absolute fluxes.

We were able to observe two fields per night, and therefore cover a full square degree on the sky. We observe each LMC field in Hα, [OIII], Continuum and B for centring purposes (and further finding charts). Each exposure was divided in 5 jittered exposures (total time between 20 and 30 min) in each filter (1 min in B). This procedure was adopted to avoid spurious identifications, and to fully cover the gaps between the 8 CCDs. Therefore, for each field, taking into account the overheads of focusing, pointing and reading (20 ×) of the CCD, an amount of ~ 2 h 30 min was needed.

4. Reductions

For interferencial imaging, the moon background is not crucial because after a 5-min exposure time, even with full moon, the sky level is of the order of 150–200 ADUs.

Preliminary reductions of the WFI data have been made, but a powerful computer was still missing at that time. Remember that a full frame is 300 Mb!

Here are the different reduction stages adopted:

– Bias substraction and FF division
– Cosmic-event removing
– Combine the 5 images per filter (not yet done)
– Frame recentring (Continuum as reference)
– Flux calibration
– Continuum frame substraction
– ([OIII]-Continuum) divided by (Hα-Continuum)
– Accurate astrometry using the ESO Starcat package facility (not yet done)

5. Results

These observations demonstrate that, as expected, we still can find a lot of new emission-line objects. Moreover, these observations provide, in the survey area, an unbiased and complete survey (range greater than 8 magnitudes).

As a first product this study, preliminary to further spectroscopic study, will lead to the publication of a catalogue with precise coordinates and good finding charts of more than 1000 emission objects (PNe, HII regions, SNR, Hα-emission stars, etc.) per square degree.

The performance of the WFI is very encouraging:

– Firstly, we were able to (easily) find the 6 known PNe present in our 4 fields, and moreover our photometry agreed within 10–20% with the fluxes derived spectroscopicaly.

– Secondly, with the calibration in fluxes, we confirm that we easily reach fluxes down to $F\alpha = 10^{-16}$ erg.cm^{-2} s^{-1}, and therefore that we are able to find objects 20–50 times fainter than the last deep survey (Jacoby 1980).

With a bigger area covered and better statistics, we will derive an unbiased PNe luminosity function.

In each of the two first 30′ by 30′ reduced fields we discovered more than 100 emission-line objects. In one field we found 2 new PNe, 8 compact HII regions and ~ 80 Hα-emission-line stars. In the other field, also 2 new PNe, 4 compact HII regions and ~140 Hα- emission line stars.

All 4 PNe are very faint and 2 of them are fully resolved (diameter > 1.0″). The PNe have fluxes of the order of 10 10^{-16} erg.cm^{-2}.s^{-1}, which one can compare to brigthest (3000 10^{-16} erg.cm^{-2}.s^{-1}) or the faintest (~ 200 10^{-16} erg.cm^{-2}.s^{-1}) PNe already known.

Figures 1 to 4 show the finding charts in both Hα and [OIII] filters.

5.1. Expected PNe number in the LMC

In 1978 Sanduleak et al. have estimated the total PNe number to 400 in the LMC (and 100 in the SMC accordingly to the LMC/SMC mass ratio equal to 4). In 1980 Jacoby determined these numbers to be 996 and 285, respectively.

The current number of known PNe in the Magellanic Clouds are respectively 282 and ~ 85 for the LMC and the SMC.

This study demonstrates that many PNe have been missed by the previous surveys and that probably a few hundred can be discovered with the current instrumentation.

In the studied area we double the known sample of PNe, therefore, we can extrapolate to find more than 250 new PNe in the LMC. Statistically, we can at least expect to find about 50–100 new faint and extended PNe in the Bar. These PNe are of particular interest because they are old, allowing to determine galaxy abundances at epoch up to 10 billions years.

6. Conclusion

The WFI has proved with this study that it is an excellent efficient instrument which can be used to survey large areas (like nearby galaxies) and still discover many faint interesting objects.

We hope that we will soon be able to cover several other square degree and determine an accurate PNe luminosity functions over this complete and unbiased sample.

The next step, with such faint objects, will be a follow-up with VLT telescopes (FORS) to obtain very good S/N spectra and derive accurate abundances.

References

Jacoby, G.H., 1980 *ApJS* **42**, 1.
P. Leisy, M. Dennefeld, 1996 *A&AS* **116**, 95.
Sanduleak, N., MacConnell, D.J., & Phillip, A.G.D., 1978, *PASP* **90**, 621.

ANNOUNCEMENTS

PERSONNEL MOVEMENTS

International Staff

(1st July 1999 – 30th September 1999)

ARRIVALS

EUROPE

ALEXOV, Anastasia (USA), Science Data Analyst/Programmer
BALESTRA, Andrea (I), Software Engineer
CESARSKY, Catherine (F), Director General
CHRISTENSEN, Lars (DK), HST Public Outreach Scientist
DELPLANCKE, Françoise (B), Physicist
DÜHRING, Margit (DK), Associate ST-ECF
FEDRIGO, Enrico (I), Software Engineer
GENNAI, Alberto (I), Control/Hardware Engineer
GORSKI, Krzyszof (PL), Archive Astronomer
IZZO, Carlo (I), Scientific Applications Developer
KIM, Tae-Sun (ROK), Fellow
MENARDI, Serge (F), Opto-Mechanical Engineer
PALSA, Ralf (D), Astronomical Data Analysis Specialist
PIRANI, Werther (I), VLT Software System Manager
PIRARD, Jean-François (B), Infrared Instrumentation Engineer
POZNA, Eszter (I), Software Engineer
TORWIE-SCHMER, Claudia (D), Accounting Assistant
WILHELM, Rainer (D), Engineer/Physicist

CHILE

CHADID, Merieme (MA), Fellow
GILLET, Gordon (D), Electronics Engineer
JONES, Heath (AUS), Fellow
LE FLOC'H, Emeric (F), Coopérant La Silla NTT

DEPARTURES

EUROPE

CONTARDO, Gertrud (D), Student
IBATA, Rodrigo (GB), Fellow
JANDER, Georg (D), Mechanical Engineer

CHILE

PIZZELLA, Alessandro (I), Fellow
SBAIHI, Marc (F), Mechanical Engineer

The ESO MESSENGER is published four times a year: normally in March, June, September and December. ESO also publishes Conference Proceedings, Preprints, Technical Notes and other material connected to its activities. Press Releases inform the media about particular events. For further information, contact the ESO Education and Public Relations Department at the following address:

EUROPEAN
SOUTHERN OBSERVATORY
Karl-Schwarzschild-Str. 2
D-85748 Garching bei München
Germany
Tel. (089) 320 06-0
Telefax (089) 3202362
ips@eso.org (internet)
URL: http://www.eso.org

The ESO Messenger:
Editor: Marie-Hélène Demoulin
Technical editor: Kurt Kjär

Printed by
J. Gotteswinter GmbH
Buch- und Offsetdruck
Joseph-Dollinger-Bogen 22
D-80807 München
Germany

ISSN 0722-6691

Local Staff (Chile)

(Until 30th September 1999)

ARRIVALS

NAVARRETE, Julio, Telescope Instrument Operator, Paranal (transferred from La Silla)
CARRASO, Cecilia, Personnel Assistant, Santiago
ZAPATA, Joel, Warehouse Administrative Assistant, Paranal
CARVAJAL, Marta, Administrative Secretary

DEPARTURES

MUÑOZ, Nelson, Electrónico, La Silla
PARADA, María, Recepcionista, Santiago
VILLANUEVA, Raúl, Ingeniero Civil, Paranal

List of Scientific Preprints

(July–September 1999)

1331. C. Mouton, K. Sellgren, L. Verstraete, A. Léger: Upper Limit on C_{60} and C_{60}^{+} Features in the ISO-SWS Spectrum of the Reflection Nebula NGC 7023. *A&A.*
1332. V. Doublier, D. Kunth, F. Courbin, P. Magain: POX 186: the Ultracompact Blue Compact Dwarf Galaxy Reveals its Nature. *A&A.*
1333. V. Doublier, A. Caulet, G. Comte: Multi-Spectral Study of a New Sample of Blue Compact Dwarf Galaxies: II.– B and R Surface Photometry of 22 Southern Objects. *A&A.*
1334. Th. Rivinius, S. Štefl, D. Baade: Central Quasi-Emission Peaks in Shell Spectra and the Rotation of Disks of Be Stars. *A&A.*
1335. F. Marchis, H. Boehnhardt, O.R. Hainaut, D. Le Mignant: Adaptive Optics Observations of the Innermost Coma of C/1995 O1. Is there a "Hale" and a "Bopp" in Comet Hale-Bopp? *A&A.*
1336. P. François, D. Briot, F. Spite, J. Schneider: Line Profile Variation and Planets Around 51 Peg and υ And. *A&A.*
1337. F. Comerón and J. Torra: A Near Infrared Study of the HII/Photodissociation Region DR 18 in Cygnus. *A&A.*
1338. S. Arnouts et al.: Measuring and Modelling the Redshift Evolution of Clustering: the Hubble Deep Field North. *M.N.R.A.S.*
1339. G. De Marchi, F. Paresce, L. Pulone: The Mass Function of Main Sequence Stars in NGC 6397 from Near IR and Optical High Resolution HST Observations. *ApJ.*
1340. F. Comerón: Vertical Motion and Expansion of the Gould Belt. *A&A.*

Contents

TELESCOPES AND INSTRUMENTATION

THE LA SILLA NEWS PAGE

REPORTS FROM OBSERVERS

ANNOUNCEMENTS